Multi-train roll waves, antidunes and bars in inclined flumes

P. Bohorquez^{a,*}, D.V. Papa^b, C. Ancey^c

^aÁrea de Mecánica de Fluidos, Departamento de Ingeniería Mecánica y Minera, Universidad de Jaén. Campus de las Lagunillas, 23071 Jaén, Spain
 ^bLadHyX, UMR 7646 du CNRS, Ecole Polytechnique, Palaiseau, France
 ^cÉcole Polytechnique Fédérale de Lausanne, 1015 Lausanne, Switzerland

Abstract

This article offers fresh theoretical insights into the phenomenon of bedforms and roll waves, highlighting their emergence from shallow water flows in a fixed-width inclined channel. Our theory is based on the Saint-Venant-Exner equations and linear stability analysis. We examine both bed and free-surface instabilities. Bed instabilities include alternate bars, antidunes, and multiple bars, while free-surface instabilities involve roll waves. We conduct a thoughtful analysis of how the transverse dimension affects flow dynamics, proving that our theoretical framework is sufficiently flexible to encompass both two-dimensional and three-dimensional bedforms, regardless of whether they are arranged in a single row or multiple rows. We compare our theoretical predictions with over 800 laboratory experiments. One significant result is the ability to predict the type of instability using three independent dimensionless parameters: the Froude number, the grain roughness relative to the water depth and the width-to-depth ratio. For Froude numbers in excess of 2, roll waves are the dominant mode, a consequence of convective instability along the free surface. For Froude numbers less than 2, two types of instability can occur along the water-sediment interface: (1) an absolute instability leading to the formation of antidunes, and (2) a convective instability giving rise to two-dimensional dunes or three-dimensional bars. Antidunes and alternate bars coexist within a specific range of the dimensionless parameters. Furthermore, a small width-to-depth ratio favors the development of two-dimensional antidunes and roll waves or three-dimensional alternate bars, whereas a large ratio leads to multi-train wave patterns. We conduct model validation by examining real-world scenarios, such as the Oroville spillway's multi-row roll waves and classic experiments on bedforms. We find that transverse flow and bed organization are sensitive to experimental and boundary conditions for convective instabilities. This means that different bedform configurations are possible within a certain range of water discharge, bed slope, channel width and grain size.

Keywords: linear stability, roll wave, antidune, alternate bar, dune, flow-transverse bedforms, Saint-Venant-Exner

1. Introduction

Open-channel flows are known to exhibit unsteady, nonuniform behavior even when water discharge remains constant over time. Grasping the reasons and mechanisms by which steady flow transitions to locally unsteady flow is crucial in hydraulics, as flow depth can vary dramatically from what is typically expected under steady uniform flow conditions (Brock, 1969, 1970). A typical example is provided by free-surface flow instabilities developing along long straight fixed beds, which are called *roll waves* (Cornish, 1907). Figure 1a shows that the Oroville Dam spillway (California, United States) can develop such large-amplitude waves (France et al., 2018; Koskinas et al., 2020). Erodible beds are another cause of flow unsteadiness: bed instabilities can develop along the water-sediment interface and affect the flow dynamics. A case in point is the formation

Email address: prmedina@ujaen.es (P. Bohorquez)

^{*}Corresponding author.

of antidunes, which alter the flow's free surface, as illustrated in Fig. 1b. There exist many other types of bedforms (Gilbert, 1914; Julien, 2010; da Silva and Yalin, 2017; Dey, 2024), which can be connected or not with free-surface instabilities. Figures 1c and d show examples of alternate and linguoid bars, respectively.

In this article, we will concentrate on roll waves, antidunes, and bars. To ensure a solid foundation, it is important to begin with concise definitions of these terms, particularly highlighting their characteristics as revealed through linear stability analysis, as opposed to the geomorphological interpretations found in a naturalist perspective:

- Roll waves are a type of free-surface instability that manifests as a series of hydraulic jumps moving downstream. Their dynamics have been studied within the framework of linear stability analysis. According to theory, the free surface of a turbulent supercritical steady-uniform flow can exhibit instability: minor disturbances of the free surface grow over time, leading to the emergence of mobile hydraulic jumps that travel at a greater speed (by a factor of 1.5) than the mean flow velocity (Dressler, 1949).
- Antidunes are a primary instability affecting erodible beds. They take the form of periodic (or nearly so) bedforms that migrate upstream. They also create free-surface waves, called stationary free-surface waves by Kennedy (1960), which are aligned more or less closely with the bed's undulations. At low discharges (for Froude numbers below 1), waves match the shapes of the bed, but at higher discharges, the surface may steepen, leading to the formation of breaking waves. In the latter case, the bed instability causes the free surface to become unstable. Antidunes are usually specific to narrow straight channels, with little variation in the bed surface elevation in the cross-stream direction; therefore, they are often considered two-dimensional bedforms.
- Bars are another form of bed instability resulting from convective instability of the moving riverbed (Federici and Seminara, 2003). Convective instability refers to localized disturbances carried by the flow, affecting only small areas rather than the entire flow. Like antidunes, bars usually appear as regular patterns in space. Unlike antidunes, however, they can migrate gradually downstream, and they exhibit three-dimensional shapes with a varying bed surface in both the streamwise and cross-stream directions. The length of a bar is usually much greater than the width of the channel. A single sequence (or train) of bars can be observed along the streambed (Fig. 1c). Parallel sequences of bars can also be observed, and this configuration is called a multiple train or multiple row of bars.

It is because the free surface or bed interface shows spatially repeating patterns that researchers have interpreted them as instabilities. The most straightforward mathematical approach for predicting the onset of instabilities is linear stability analysis, which studies how the flow responds to minor harmonic disturbances. This article will follow this approach.

We feel it is essential to make a side note here that will aid in grasping the following mathematical developments. Analyzing the stability of fixed-width channels requires us to look at harmonic disturbances differently, based on whether we focus on the flow direction or the transverse direction. To describe what happens in the flow direction, we will use the wavenumber k_x , which is defined as the ratio of the channel width to the streamwise wavelength multiplied by a factor of 2π . To describe the behavior in the transverse direction, we will use the lateral Fourier mode m, which is a multiple of the transverse wavenumber k_y and can be defined as four times the ratio

of channel width to the lateral wavelength. The reason for this differential treatment is that the number of wavelengths in the transverse direction is finite (m is therefore a discrete variable). In contrast, the number of wavelengths in the flow direction is not fixed a priori (k_x is therefore a continuous variable).

1.1. Roll waves

The earliest description of roll waves was recorded by Cornish (1907), who observed them in an artificial channel at Merligen, Switzerland. Later, Thompson (1968) documented the formation of one-dimensional roll waves in a large flume at the Santa Anita spillway in Arcadia, California, while Brock (1969, 1970) built a rectangular aluminium channel to study their spontaneous formation in the laboratory. More recently, experimenters analyzed how steep slopes (Guo, 1999; Chan et al., 2025), sediment transport (Zhao et al., 2015), and overland flows (Wang et al., 2021) affect their dynamics and conditions of occurrence. In all these studies, the flow regime was turbulent.

Cornish, Thompson and Brock mentioned the formation of one-dimensional hydraulic jumps that extended across the entire channel width, but did not report other flow patterns. Other authors derived a (now classic) theoretical criterion for observing roll waves: by neglecting the cross-channel flow component and considering simplified flow conditions, they showed that single roll waves are a traveling-wave solution of the Saint-Venant equations (Jeffreys, 1925; Dressler, 1949; Hwang and Chang, 1987; Yu and Kevorkian, 2000; Chang et al., 2000; Di Cristo and Vacca, 2005). This theoretical framework was subsequently refined, for example, by incorporating turbulent stresses into the momentum balance equation and demonstrating that turbulent viscosity introduces a cutoff in the wavenumber spectrum (Needham and Merkin, 1984; Balmforth and Vakil, 2012; Bohorquez and Ancey, 2015). Although more sophisticated theoretical frameworks have been developed in the last few decades to study the stability of shallow flows (Colombini and Stocchino, 2012), we believe that there is still room and interest for a model based on a set of relatively simple equations (the Saint-Venant equations) capable of predicting the formation of roll waves. Our own experience has shown that this simplified framework allows for the numerical simulation of entire nonlinear processes of growth, coarsening, and saturation at affordable computational costs (e.g., Di Cristo et al., 2008; Bohorquez, 2010; Cao et al., 2015). In the present article, we extend previous work by demonstrating that turbulent shallow flows in sufficiently large channels can develop free-surface instabilities that are more complex than the typical solitary roll wave; this extension is based on the linear stability analysis of the two-dimensional Saint-Venant equations.

1.2. Antidunes

The formation of antidunes in laboratory flumes has been a subject of interest since the earliest flume experiments conducted by Gilbert (1914) and Kennedy (1960). This topic has been of continued interest, as is evident from the subsequent studies of Simons et al. (1963), Guy et al. (1966), Cao (1985), Recking et al. (2009), Núñez González and Martín-Vide (2011), Cartigny et al. (2014), Mettra (2014), Inoue et al. (2020), Pascal et al. (2021), and others. Most of these experiments have presented antidunes as bedforms with simple characteristics: they are periodic patterns that migrate upstream, remain in phase with the surface, and present a uniform cross-sectional profile across the entire width of the channel. These characteristics only apply when the channel is narrow. In wider channels, antidunes exhibit much more complex patterns. Simons et al. (1963) reported on multiple row antidunes and three-dimensional antidunes. More recently, Yokokawa et al. (2010) highlighted a cycle of creation/destruction, the dynamics of which are controlled by the interaction between bedforms and surface waves. When two-dimensional antidunes initially form in a wide

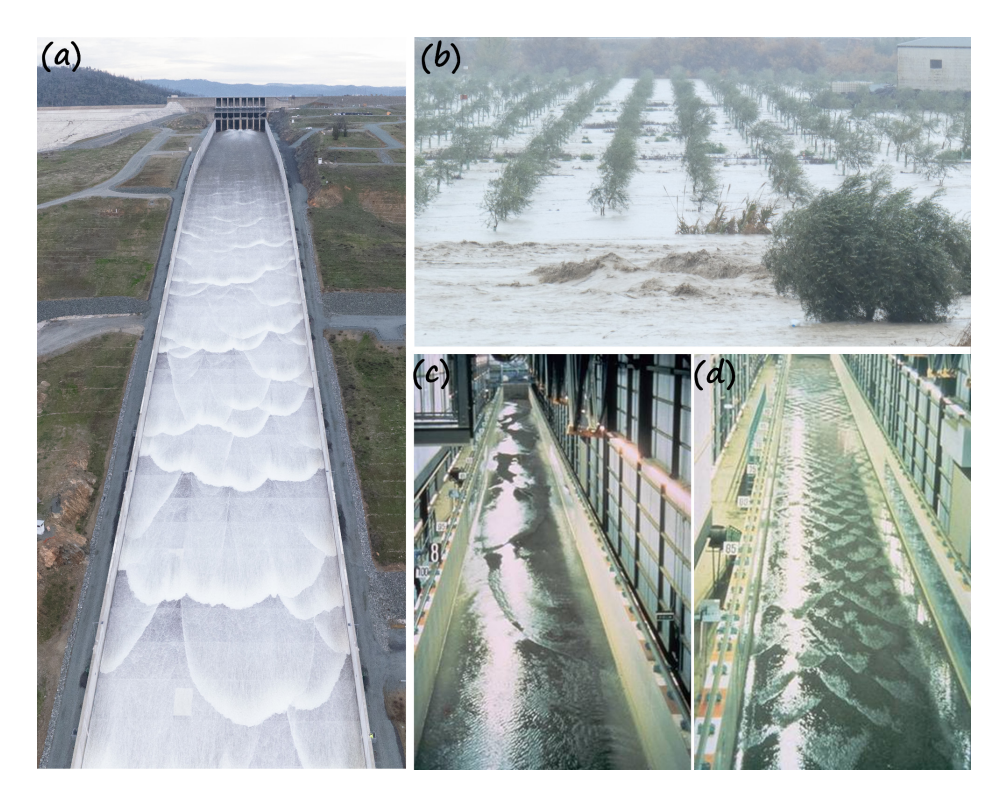


Fig. 1: (a) Roll waves with multiple transverse modes in the Oroville Dam's 931-m-long and 54.5-m-wide spillway (California, United States) recorded on 31 January 2024 (California Department of Water Resources: Galleries, 2025). (b) Three-dimensional surface water waves beneath which antidunes form during a flood in the Salado de Porcuna River (Jaén, Spain) on 20 December 2019. Upstream views of (c) alternate bars and (d) linguoid bars in a recirculating flume, 4 m wide and 160 m long (Tsukuba University, Japan), at 73 min and 7 min after start of flow in Run 80 by Ikeda (1983, Fig. 3-26).

channel, they create surface waves on either side of the channel, which are oblique to the main flow direction. These waves slowly shape the antidunes into a three-dimensional form. At some point, however, the surface waves become locally steep, forcing the antidunes back to their original shape. And so the cycle begins again. According to Carling and Shvidchenko (2002), oblique hydraulic jumps from flume sidewalls were first observed by Robillard (1965) in supercritical flows over a wavy fixed bed that resembled two-dimensional antidunes. Inoue et al. (2020) observed the formation of triple-train antidunes, which evolved into a single train of three-dimensional antidunes. Subsequently, multiple-row and three-dimensional antidunes have formation mechanisms that differ from those governing solitary, two-dimensional antidunes.

Most theorists have so far overlooked the flow dynamics in the cross-stream direction and the influence of the channel width (Bose and Dey, 2009; Camporeale and Ridolfi, 2011; Andreotti et al., 2012; Charru et al., 2013; Deigaard, 2006; Di Cristo et al., 2006; Vesipa et al., 2012; Bohorquez and Ancey, 2015; Greco et al., 2017; Reynolds, 1965; Gradowczyk, 1968; McLean, 1990; Balmforth and Provenzale, 2001; Bohorquez et al., 2019), which severely limits the modeling capability when considering three-dimensional or multi-row antidunes. Our linear stability analysis overcomes this limitation by providing predictions of multi-row instabilities in agreement with experimental observations.

1.3. Bars

Bars are periodic sequences of riverbed erosion and deposition. When they form spontaneously, they are called *free bars*, whereas if they are caused by an external force, such as a bridge pier, they are called *forced bars*. In this work, we are interested in free bars, which are downstream-migrating bedforms, the characteristics of which are proportional to the channel width and the flow depth (da Silva and Yalin, 2017). Bars can appear in a wide range of flow configurations in the field and the laboratory (Ikeda, 1973, 1975), the simplest of them being *alternate bars*, also called a one-row bar or a single-row bar (see Fig. 1c). They are characterized by an alternating sequence of elongated deposition fronts and scour holes on both sides of the stream. Multiple bars have been reported on much wider channels than those exhibiting alternate bars (Yalin, 1977). They usually take the form of a series of alternate bars that repeat across the width of the channel and, depending on the number of rows, they are given different names (e.g., mid-channel bar, lateral bars, and rhomboidal bars). Some authors have called them *linguoid bars*, and they form a preliminary stage of river braiding (Fujita, 1989; Ashmore, 2013).

Alternate bars have been the subject of extensive research over the past fifty years, and there is thus a substantial literature devoted to experiments of alternate bars (e.g., Fujita and Muramoto, 1982; Ikeda, 1984; Jaeggi, 1984; Fujita and Muramoto, 1985; Garcia and Niño, 1993; da Silva, 1991; Lanzoni, 2000; Boraey, 2014; Garcia Lugo et al., 2015; Cheng and da Silva, 2023). Theoretically, they have been studied using linear-stability analysis (e.g., Callander, 1969; Fredsøe, 1978; Kuroki and Kishi, 1984; Parker, 1976; Blondeaux and Seminara, 1985; Colombini et al., 1987; Nelson, 1990; Federici and Seminara, 2003; Iwasaki et al., 2016; Mahato et al., 2021), dimensional principles (da Silva and Yalin, 2017; Cheng and da Silva, 2023) and using numerical simulations (e.g., Duró et al., 2016; Huang et al., 2023). These studies have demonstrated that the standard Exner equation, combined with the two-dimensional shallow-water equations, is capable of predicting the formation of alternate bars in the saturated, nonlinear regime. Non-capacity bedload models also yield accurate predictions of the alternate bar dimensions, as shown numerically by Qian et al. (2017) and Guan and Liang (2017). Unlike alternate bars, multiple bars have rarely been studied because of the extreme difficulty of replicating them in the laboratory. Using an 8-m-long 80-cmwide flume, Ikeda (1973) noted that multiple bars developed only in seven of almost a hundred experimental runs, when the cross-section aspect ratio was large enough. Many experiments were also carried out, compiled and described in detail in Fujita and Muramoto (1988) and Fujita (1989), who ran nearly 30 tests in different experimental setups from 15 m to 43 m in length, and 1.8 m to 3 m in width. Ahmari and Da Silva (2011) reviewed experiments on multiple bars, comparing them with those on alternate bars, meandering and braiding channels, and derived an empirical criterion for the occurrence of multiple bars.

1.4. Bedform diagram and key dimensionless numbers

The study of bed and free-surface instabilities is important not only from a theoretical point of view, but also for practical engineering applications. Indeed, as large bedforms influence sediment transport and the channel dynamics, safe design of hydraulic structures requires taking them into account (Bradley and Venditti, 2017). Safe design is not only a matter of characterizing bedform geometries, but also of determining their conditions of existence (García, 2007). The study of instabilities is also useful in other disciplines; a good example is fluvial geomorphology, where the bedform type can be used as a proxy for flow variables and regime (Carling, 2013; Jacobson et al., 2016).

One practical question is how to synthesize information on instabilities best. Most scientists have chosen to use diagrams for predicting bedform type and occurrence. These diagrams, known as bedform predictors or charts (Yalin, 1977), are primarily two-dimensional representations based on dimensionless numbers. In this article, we aim to generalize these diagrams through the introduction of three-dimensional representations that enable the classification of bedforms (antidunes, bars, and dunes) and free-surface flow instabilities (roll waves) according to flow characteristics. In contrast to previous work, the diagrams are based on linear-stability theory and validated through comparison with flume experiments.

The role of dimensionless numbers in the instabilities cited above has been recognized for several decades. The Froude number was identified as the key dimensionless parameter characterizing the development of roll waves in turbulent streams, as shown in the earliest linear-stability studies of Jeffreys (1925) and Dressler (1949). It also controls the dune-antidune transition (Anderson, 1953; Kennedy, 1963). By analyzing laboratory and field data of antidunes, dunes, ripples and chutes/pools, Athaullah (1968) demonstrated the role of the grain roughness relative to the water depth in determining the bedform type. Kinoshita (1957) identified the width-to-depth ratio—also called aspect ratio—as an additional key parameter for alternate bar formation. Later, Callander (1969) and Muramoto and Fujita (1977) applied linear-stability and self-similarity theories (Barenblatt, 1996), respectively, for studying the role of this ratio. Despite these significant theoretical advances, it is worth noting that there is still no unified shallow-water theory for the formation of all these instabilities involving all the relevant flow and sediment parameters.

1.5. Contribution and organization of the article

Compared to our previous linear stability analyses (Bohorquez and Ancey, 2015; Bohorquez et al., 2019), the novelty of the present study is the addition of an extra spatial dimension (i.e., the channel width), which results in a third dimensionless parameter: the width-to-depth ratio. In our earlier articles, we considered the role of the relative grain roughness and the Froude number in determining the two-dimensional bedform and free-surface instabilities, namely dunes or antidunes, and roll waves, respectively. Here, we extend the ability to predict other instabilities along both the sediment interface and the water surface by considering the effects of the width-to-depth ratio on flow stability. The new bedform types associated with the primary instability of the sediment include bars and antidunes with various configurations such as alternate bars, rhomboid bars, multi-row bars, three-dimensional antidunes, and multi-train antidunes. Additionally, we demonstrate that roll waves are a primary water surface instability that can develop from clear water flows as well as flows over a mobile sediment bed with different transverse shapes (including uniform, alternate, and multiple rows). All these phenomena have been observed experimentally in the field and through classical flume studies, as shown in Fig. 1.

The article is organized as follows: first, we present the two-dimensional morphodynamic model and formulate the linear stability problem in Section 2.1; then, we analyze the capability of this model to capture the formation of roll waves, antidunes and bars in Sections 3.1, 3.2 and 3.3, respectively; subsequently, based on available experimental data in flumes (Section 3.4), we review the relevant dimensionless parameters that control the formation of dunes and antidunes, roll waves, and bars, which allows us to propose a novel three-dimensional bedform diagram in agreement with the neutral surfaces of the linear stability theory; finally, conclusions are drawn in Section 4.

2. Formulation of the problem

2.1. Morphodynamic model

We use the Saint-Venant equations, also referred to as the shallow-water equations, to describe the motion of the water phase. Regardless of the number of spatial dimensions considered in the model (i.e. one- or two-dimensional flow) or the coordinate system employed to express the governing equations (Cartesian or curvilinear), the mass and momentum balance equations can be derived by depth-averaging the Navier–Stokes equations for clear water, which leads to the following compact form (Dey, 2024):

$$\frac{\partial \widehat{\eta}}{\partial \widehat{t}} + \widehat{\nabla} \cdot (\widehat{\eta} \,\widehat{\boldsymbol{u}}) = 0 \,, \tag{1}$$

$$\frac{\partial \widehat{\eta} \, \widehat{\boldsymbol{u}}}{\partial \widehat{t}} + \widehat{\nabla} \cdot (\widehat{\eta} \, \widehat{\boldsymbol{u}} \, \widehat{\boldsymbol{u}}) + \widehat{\nabla} \left(\frac{\widehat{g} \, \widehat{\eta}^2}{2} \right) = -\widehat{g} \, \widehat{\eta} \, \widehat{\nabla} \widehat{\boldsymbol{z}} - \frac{\widehat{\boldsymbol{\tau}}_b}{\widehat{\rho}} + \widehat{\nabla} \cdot \left(\widehat{\eta} \widehat{\boldsymbol{\nu}} \cdot \widehat{\nabla} \widehat{\boldsymbol{u}} \right) \,, \tag{2}$$

where dimensional quantities are denoted by a hat, \hat{t} is time, $\hat{\eta}$ is the water depth measured along the vertical coordinate, \hat{u} is the depth-averaged velocity, \hat{z} is the bed elevation, and \hat{g} is the acceleration due to gravity. The source terms in the momentum equation involve the bed slope $\hat{\nabla}\hat{z}$, the bottom shear stress per unit density $\hat{\tau}_b/\hat{\rho}$, in which $\hat{\rho}$ denotes water density, and the parabolic term $\hat{\nabla}\cdot(\hat{\eta}\hat{\nu}\cdot\hat{\nabla}\hat{u})$, which is the depth-averaged divergence of the turbulent normal stress (in the flow direction) (Cea et al., 2007; Cao et al., 2015). This term, which does not appear in the standard Saint-Venant equations, is justified whenever turbulence or velocity nonuniformity affects the flow dynamics; as shown by Cao et al. (2015), this situation is met, for instance, when free-surface instabilities (e.g., roll waves) occur. This latter term is therefore of crucial importance for correctly predicting the onset of linear instability for mobile beds. Indeed, in the absence of a diffusive term in the momentum balance equation, the bottom shear stress is in phase with the velocity, and in this case, the bed remains stable. In the following, we will use a Boussinesq-like parametrization to describe the dependence of the normal stress on the depth-averaged velocity, and in this context, $\hat{\nu}$ is the eddy viscosity.

The most common way of incorporating the effect of bedload transport on flow has long been to use an Exner equation (reflecting the mass balance of the bed) with an empirical equation (such as the Meyer-Peter-Müller equation) relating sediment transport rate to bed shear stress. Charru and colleagues have shown that this assumption is too inaccurate if the goal is to calculate the formation and migration of morphological structures. For example, for a dune, particle entrainment is more pronounced on the upstream face than on the downstream face, and the opposite is true when deposition is considered; it is thus the difference in behavior between upstream and downstream faces that explains (qualitatively) the migration of dunes (Charru, 2006; Charru et al., 2013). Charru concluded that bedload transport rates must be modulated to account for the effect of bed topography on mean flow, and a simple way to introduce modulation is to include a bedload transport relaxation equation. Subsequent work based on a stochastic analysis of particle motion confirmed that bedload transport and bed stresses are not univocally related (Ancey and Heyman, 2014; Furbish et al., 2017). In this review article, we generalize the set of equations obtained by Ancey et al. (2015) and the relevance of which was shown for describing the bedload transport dynamics for supercritical flows (Bohorquez and Ancey, 2015, 2016; Bohorquez et al., 2019). In this approach, bedload transport rate is not calculated directly. Instead, one computes the volume of moving particles per unit streambed area, a variable referred to as "particle activity" by Furbish et al. (2012). Ancey et al. (2015) showed that the time variations in the ensemble average of particle activity was described by an advection-diffusion equation. When generalizing this result to two-dimensional flows, we end up with the following advection-diffusion equation:

$$\frac{\partial \widehat{\gamma}}{\partial \widehat{t}} + \widehat{\nabla} \cdot (\widehat{\boldsymbol{u}}_p \widehat{\gamma}) - \widehat{\nabla} \cdot (\widehat{\boldsymbol{\alpha}} \cdot \widehat{\nabla} \widehat{\gamma}) = \widehat{\kappa} (\widehat{\gamma}_{ss} - \widehat{\gamma}) , \qquad (3)$$

where \hat{u}_p is the mean velocity of moving particles, and $\hat{\alpha}$ is the particle diffusivity tensor. Equation (3) describes how sediment particles are advected by the water flow (at velocity \hat{u}_p), spread along the bottom of the channel, and are entrained or deposited depending on the sign of $\hat{\gamma}_{ss} - \hat{\gamma}$. The constant parameter $\hat{\kappa}$ in Eq. (3) determines the time and spatial scales at which $\hat{\gamma}$ reaches the equilibrium value $\hat{\gamma}_{ss}$ (Bohorquez and Ancey, 2016). As a first approximation, the bedload transport rate can estimated as $\hat{\gamma}\hat{u}_p$ within this framework (Furbish et al., 2012; Ancey et al., 2015). Using Eq. (3), we can express the Exner equation as:

$$(1 - \zeta_b) \frac{\partial \widehat{z}}{\partial \widehat{t}} = \widehat{\kappa} \left(\widehat{\gamma} - \widehat{\gamma}_{ss} \right) , \tag{4}$$

in which ζ_b is the bed porosity. This equation describes the time variations in the bed elevation due to particle entrainment and deposition.

With regards to terminology, the historical approach (the one founded on empirical equations such as the Meyer-Peter-Müller equation) is referred to as equilibrium flow theory, since it assumes that sediment transport rates and particle activity adapt instantaneously to any change in water flow, and that sediment transport takes place at its maximum capacity (Wainwright et al., 2015); mathematically, this means that the sediment transport rate and particle activity are one-to-one functions of the bed shear stress or, in non-dimensional form, the Shields number:

$$Sh = \frac{|\widehat{\tau}_b|}{\widehat{\rho}(s-1)\widehat{g}\widehat{d}},\tag{5}$$

where \hat{d} is the mean particle diameter and the constant parameter s is the particle-to-water density ratio. Conversely, the approach taken in this article is referred to as the non-equilibrium flow theory, since no assumption is made about the equilibrium state of sediment transport, and thus generally, for a given water flow rate, different values of bedload transport rates are possible.

2.2. Closure equations

We present here the equations used to close the governing equations. Before we start, it should be noted that: (i) our choice is not unique, but corresponds to the choice of parameters that seemed to us to be the most relevant, and that; (ii) the physics of out-of-equilibrium phenomena is still imperfectly known even for well-studied phenomena such as flow resistance on gravel beds. We have not explored the parametric dependence of the results described below on these closure equations, as this is beyond the scope of the study.

For evaluating the hydraulic resistance term $\hat{\tau}_b$ in Eq. (2), we use the Darcy–Weisbach friction factor f:

$$\frac{\widehat{\boldsymbol{\tau}}_b}{\widehat{\rho}} = \frac{f}{8}\widehat{\boldsymbol{u}}|\widehat{\boldsymbol{u}}|. \tag{6}$$

We furthermore assume that: (i) a channel width \widehat{B} is much larger than the flow depth $\widehat{\eta}_0$, which makes it possible to neglect the wall shear stresses with respect to the mean bed shear stress;

October 11, 2025

(ii) the friction factor depends solely on relative submergence $\widehat{\eta}/\widehat{d}$, and is independent of bedforms (form resistance) and bedload transport. To evaluate the friction factor, f, we use a Keulegan-type equation:

$$\frac{1}{\sqrt{f}} = 2.03 \log \left(\frac{12.2\widehat{\eta}}{\widehat{k}_s} \right), \tag{7}$$

where the bed roughness size \hat{k}_s is set to 3.3 \hat{d} ; other choices are possible, but none of them has so far proved better than the others, given the large variability of the experimental conditions (López and Barragán, 2008).

We use the Boussinesq model for estimating the eddy viscosity. This model involves assuming that turbulence is isotropic and the eddy viscosity depends solely on the friction velocity $\hat{u}_* = \sqrt{\hat{\tau}_b/\hat{\rho}}$ and depth $\hat{\eta}$:

$$\widehat{\boldsymbol{\nu}} = c_t \,\widehat{\boldsymbol{\eta}} \,\widehat{\boldsymbol{u}}_* \,\mathbf{I} = c_t \,\widehat{\boldsymbol{\eta}} \,|\widehat{\boldsymbol{u}}| \,\sqrt{\frac{f}{8}} \mathbf{I}$$
(8)

where $c_t \sim O(1)$ is a turbulent constant parameter and **I** is the identity tensor. We set $c_t = 1$ for the sake of simplicity.

We evaluate the particle diffusivity $\hat{\alpha}$ in Eq. (3) as $\hat{\alpha} = \hat{\nu}/Sc$, where Sc denotes the turbulent Schmidt number; here, we assume that Sc = 0.5. For the rest of the parameters, we follow Bohorquez et al. (2019); we simplify the empirical equations used for closing Eq. (3). The particle velocity can be related to the fluid by assuming that both vector fields are collinear, and their magnitudes can be related to each other using:

$$a = \frac{|\widehat{\boldsymbol{u}}_p|}{|\widehat{\boldsymbol{u}}|}.$$

We set the sediment-to-water velocity ratio to its upper limit: a = 1. We assume that the steady-state particle activity can be estimated using the relationship: $\hat{\gamma}_0 = 14 \hat{d} (1 - \zeta_b) (Sh_0 - Sh_{cr})$, where Sh_{cr} is the Shields number related to incipient sediment motion. The relaxation time can be evaluated as $\hat{\kappa} = 0.1[(s-1)\hat{g}/\hat{d}]^{1/2}$. We assume that particles are round sand grains, and we therefore take $\zeta_b = 0.4$ for bed porosity, and s = 2.65 for the density ratio.

2.3. Dimensionless control parameters

We consider the following characteristic dimensions: a channel-width scale \widehat{B} , a length scale $\widehat{\eta}_0$, a velocity scale \widehat{u}_0 , and a characteristic particle activity $\widehat{\gamma}_0$, corresponding to a one-directional uniform flow (in the x-direction). The scaled variables involved in the Saint-Venant–Exner equations (1)–(4) are then:

$$x = \frac{\widehat{x}}{\widehat{B}}, \quad t = \frac{\widehat{t}}{\widehat{B}/\widehat{u}_0}, \quad u = \frac{\widehat{u}}{\widehat{u}_0}, \quad \eta = \frac{\widehat{\eta}}{\widehat{\eta}_0}, \quad \gamma = \frac{\widehat{\gamma}}{\widehat{\gamma}_0}, \quad z = \frac{\widehat{z}}{\widehat{\eta}_0}.$$
 (9)

The subscript 0 refers to the base-flow conditions.

Substituting Eqs. (9) into (1)–(4) and taking into account that $\nabla = \widehat{B} \widehat{\nabla}$, the dimensionless forms of the governing equations for the water depth $\eta(x,t)$ and velocity field $\boldsymbol{u}(x,t)$, the bed

elevation z(x,t), and the mean particle activity $\gamma(x,t)$, read:

$$\frac{\partial \eta}{\partial t} + \nabla \cdot (\eta \, \boldsymbol{u}) = 0 \,, \tag{10}$$

$$\frac{\partial \eta \boldsymbol{u}}{\partial t} + \nabla \cdot (\eta \boldsymbol{u} \boldsymbol{u}) + \frac{1}{\mathcal{F} \tau^2} \left[\nabla \left(\frac{\eta^2}{2} \right) + \eta \nabla z \right] = -\beta \frac{f}{8} \boldsymbol{u} |\boldsymbol{u}| + \frac{1}{\beta} \nabla \cdot (\eta \boldsymbol{\nu} \cdot \nabla \boldsymbol{u}) , \qquad (11)$$

$$\frac{\partial \gamma}{\partial t} + \nabla \cdot (\boldsymbol{u}_p \gamma) - \frac{1}{\beta} \nabla \cdot (\boldsymbol{\alpha} \nabla \gamma) = \beta \, \kappa_\eta \, (\gamma_{ss} - \gamma) \,\,, \tag{12}$$

$$\frac{\partial z}{\partial t} = \beta \,\kappa_{\gamma} \left(\gamma - \gamma_{ss} \right) \,. \tag{13}$$

Our approach involves three dimensionless parameters, namely the Froude number

$$\mathcal{F}\tau = \frac{\widehat{u}_0}{\sqrt{\widehat{g}\,\widehat{\eta}_0}}\,,\tag{14}$$

the relative roughness, defined as the ratio of the mean diameter of the grains \hat{d} to the flow depth $\hat{\eta}_0$ and which represents the inverse of the relative submergence (which is more common)

$$d = \frac{\widehat{d}}{\widehat{\eta}_0}, \tag{15}$$

and the aspect ratio of the cross-section

$$\beta = \frac{\widehat{B}}{\widehat{\eta_0}} \,. \tag{16}$$

Under steady state conditions, relative grain roughness d and friction factor f_0 are related to bed slope S:

$$S = \frac{f_0}{8} \mathcal{F} \epsilon^2 \quad \text{with} \quad f_0 = \frac{1}{4} \log^{-2} \left(\frac{\ell}{3.71} \right) . \tag{17}$$

The base flow hydraulic constants $\{\widehat{\eta}_0, \widehat{u}_0\}$ are obtained from the bed slope S, the channel width \widehat{B} , the bed roughness \widehat{d} and, for instance, the water discharge \widehat{Q} by solving the implicit equations:

$$\widehat{u}_0^2 = \frac{8\,\widehat{g}\,S}{f_0}\,\widehat{\eta}_0 \quad \text{and} \quad \widehat{Q} = \widehat{\eta}_0\,\widehat{u}_0\,\widehat{B}\,, \tag{18}$$

where the friction factor can be estimated using Eq. (17). It should be noted that, when analyzing particular flume experiments, it may be more appropriate to use f_0 values specifically calibrated from these experiments to improve accuracy. After determining $\hat{\eta}_0$ and \hat{u}_0 , we can evaluate the key dimensionless parameters \mathcal{F}_{ℓ} , \mathcal{A} and β using, respectively, Eqs. (14), (15) and (16).

The scaled eddy viscosity tensor ν , the dimensionless relaxation rates κ_{η} and κ_{γ} , and the particle diffusivity tensor α are defined by:

$$\boldsymbol{\nu} = \frac{\widehat{\boldsymbol{\nu}}}{\widehat{\eta}_0 \, \widehat{u}_0} \,, \quad \kappa_{\eta} = \frac{\widehat{\kappa} \, \widehat{\eta}_0}{\widehat{u}_0} \,, \quad \kappa_{\gamma} = \frac{\widehat{\kappa} \, \widehat{\gamma}_0}{(1 - \zeta_b) \, \widehat{u}_0} \,, \quad \boldsymbol{\alpha} = \frac{\widehat{\boldsymbol{\alpha}}}{\widehat{\eta}_0 \, \widehat{u}_0} \,. \tag{19}$$

Using these scales, we find that $\kappa_{\eta} = 0.1 (s-1)^{1/2}/(\Im \iota \ell^{1/2})$ and $\kappa_{\gamma}/\kappa_{\eta} \approx 14 \ell (Sh - Sh_{cr})$ for $\zeta_b = 0.4$ and s = 2.65, while the steady-state (or saturated) particle activity, referred to as γ_{ss} in Eqs. (12)–(13) is given by:

$$\gamma_{ss}(Sh) = \begin{cases} \frac{Sh - Sh_{cr}}{Sh_0 - Sh_{cr}} & \text{if} \quad Sh \ge Sh_{cr}, \\ 0 & \text{if} \quad Sh < Sh_{cr}. \end{cases}$$
 (20)

October 11, 2025

In our approach, the steady-state particle activity γ_{ss} is a conditional function of the Shields number because we assume that there is no bedload transport when Sh is below the threshold of incipient motion Sh_{cr} ; in practice, this assumption may lead to inaccurate estimates of bedload transport rates (Ancey and Recking, 2023), but it is considered sufficiently accurate for the present study. In sand- and gravel-bed rivers in the hydraulically rough turbulent regime, the critical Shields number is typically $Sh_{cr} = 0.02$ (Julien, 2010). The Shields number Sh (5) can now be rewritten as a function of $\mathcal{F}_{\mathcal{I}}$ (14) and \mathcal{J} (15) using Eqs. (6) and (9):

$$Sh = \frac{f \,\widehat{u}_0^2 \,|\boldsymbol{u}|^2}{8 \,(s-1) \,\widehat{g} \,\widehat{\eta}_0 \,\ell} = \frac{f \,\mathcal{F}\tau^2}{8 \,(s-1) \,\ell} \,|\boldsymbol{u}|^2 \,. \tag{21}$$

The base-flow Shields number Sh_0 can be calculated by setting |u| = 1 in Eq. (21) and using Eq. (17):

$$Sh_0 = \frac{f_0 \mathcal{F}r^2}{8(s-1) d} = \frac{S}{(s-1) d}.$$
 (22)

2.4. Derivation of the eigenvalue problem

We consider the linear stability analysis of a steady, uniform flow down an erodible bed inclined at a constant slope S with respect to the horizontal. Given the scales (9), the base-flow solutions to the dimensionless Saint-Venant–Exner equations (10)–(13) are: $\eta_0 = 1$, $u_0 = \mathbf{e}_x$, $\gamma_0 = 1$ and $z_0 = -\beta S x$.

Substituting the expansions $(\eta, \boldsymbol{u}, \gamma, z) = (\eta_0, \boldsymbol{u}_0, \gamma_0, z_0) + \epsilon (\eta_\epsilon, \boldsymbol{u}_\epsilon, \gamma_\epsilon, z_\epsilon)$ into the scaled governing equations (10)–(13), with $\boldsymbol{u}_\epsilon = u_\epsilon \mathbf{e}_x + v_\epsilon \mathbf{e}_y$, expanding f and γ_{ss} in a Taylor series about the base flow, and retaining only the terms of the order $O(\epsilon)$, we end up with the linear perturbation equations:

$$\frac{\partial \eta_{\epsilon}}{\partial t} + \frac{\partial \eta_{\epsilon}}{\partial x} + \frac{\partial u_{\epsilon}}{\partial x} + \frac{\partial v_{\epsilon}}{\partial x} = 0, \qquad (23)$$

$$\mathcal{F}^{2}\left[\frac{\partial u_{\epsilon}}{\partial t} + \frac{\partial u_{\epsilon}}{\partial x} - \frac{\nu}{\beta}\left(\frac{\partial^{2} u_{\epsilon}}{\partial x^{2}} + \frac{\partial^{2} u_{\epsilon}}{\partial y^{2}}\right)\right] + \frac{\partial \eta_{\epsilon}}{\partial x} + \frac{\partial z_{\epsilon}}{\partial x} = \beta S\left(\eta_{\epsilon} - 2u_{\epsilon}\right),\tag{24}$$

$$\mathcal{F}\tau^{2} \left[\frac{\partial v_{\epsilon}}{\partial t} + \frac{\partial v_{\epsilon}}{\partial x} - \frac{\nu}{\beta} \left(\frac{\partial^{2} v_{\epsilon}}{\partial x^{2}} + \frac{\partial^{2} v_{\epsilon}}{\partial y^{2}} \right) \right] + \frac{\partial \eta_{\epsilon}}{\partial y} + \frac{\partial z_{\epsilon}}{\partial y} = -\beta \, S \, v_{\epsilon} \,, \tag{25}$$

$$\frac{\partial \gamma_{\epsilon}}{\partial t} + a \left(\frac{\partial u_{\epsilon}}{\partial x} + \frac{\partial \gamma_{\epsilon}}{\partial x} + \frac{\partial v_{\epsilon}}{\partial y} \right) - \frac{\alpha}{\beta} \left(\frac{\partial^{2} \gamma_{\epsilon}}{\partial x^{2}} + \frac{\partial^{2} \gamma_{\epsilon}}{\partial y^{2}} \right) = \beta \kappa_{\eta} \left(u_{\epsilon} \gamma_{ss}' - \gamma_{\epsilon} \right) , \tag{26}$$

$$\frac{\partial z_{\epsilon}}{\partial t} = \beta \, \kappa_{\gamma} \left(\gamma_{\epsilon} - u_{\epsilon} \, \gamma_{ss}' \right) \,, \tag{27}$$

with $\nu = c_t S^{1/2}/\mathcal{F}r$ and $\alpha = \nu/Sc$.

It is worth noting that: (i) the term f' was neglected in Eqs. (24)–(26) because $\ell \ll 1$ (Bohorquez et al., 2019), and; (ii) the γ'_{ss} term in Eqs. (26)–(27) influences the stability of the base flow because it represents the linear response of γ_{ss} to a small change in the flow velocity. Using Eq. (20), we obtain:

$$\gamma'_{ss} = \frac{\mathrm{d}\gamma_{ss}}{\mathrm{d}u} \bigg|_{\substack{u_0 \\ n_0}} = \frac{\mathrm{d}\gamma_{ss}}{\mathrm{d}Sh} \bigg|_{Sh_0} \frac{\mathrm{d}Sh}{\mathrm{d}u} \bigg|_{u_0} = \frac{2Sh_0}{Sh_0 - Sh_{cr}}.$$
 (28)

October 11, 2025

Another interesting point to note is that the linearized perturbation equations (23)–(27) lead to the same equations as those of the one-dimensional theory of Bohorquez et al. (2019) for dunes and antidunes, when we set $\beta = 1$ (i.e. $\hat{B} = \eta_0$) and $v_{\epsilon} = 0$.

The solution to the linear perturbation equations (23)–(27) in the temporal stability analysis can be written as:

$$(\eta_{\epsilon}, u_{\epsilon}, v_{\epsilon}, \gamma_{\epsilon}, z_{\epsilon})^{T} = (H_{\epsilon}, U_{\epsilon}, V_{\epsilon}, G_{\epsilon}, Z_{\epsilon})^{T} \exp[i(k_{x} x + \frac{\pi}{2} m \ y - \omega t)]$$
(29)

where the real longitudinal wavenumber is denoted by k_x , the integer value of m is the lateral Fourier mode and the complex frequency is $\omega = \omega_r + \mathrm{i}\,\omega_i$ (Schmid and Henningson, 2001). The dimensionless wavenumber k_x is defined from the dimensional wavelength $\hat{\Lambda}_x$ by:

$$k_x \equiv 2\pi \frac{\widehat{B}}{\widehat{\Lambda}_x} \,. \tag{30}$$

The analysis of normal modes (29) takes into account that the longitudinal coordinate x is unbounded, and therefore k_x can take any real value. By contrast, the cross-stream coordinate y is bounded by the limits [-0.5, 0.5], and therefore, the wavenumber is

$$k_y \equiv 2\pi \frac{\widehat{B}}{\widehat{\Lambda}_y} = \frac{\pi}{2} m, \qquad (31)$$

which yields the dimensional wavelength $\hat{\Lambda}_y = 4 \hat{B}/m$ across the channel width.

It should be noted that whereas bedforms such as bars have been investigated using a Fourier decomposition in terms of sinusoidal functions depending on the even or odd values of the Fourier mode m (e.g., Nelson, 1990), other bed instabilities such as antidunes have not been investigated within this framework beforehand even when three-dimensional antidunes and multiple trains of antidunes have been observed in classic flume experiments (Kennedy, 1960; Guy et al., 1966). Similarly, theoretical studies of water-surface instability (roll waves) have neglected the flow's multi-modal nature observed in wide spillways, and assumed a one-dimensional flow (in other words, the transverse direction was ignored). For consistency with previous studies on bars, we can match the standard bar decomposition (Callander, 1969; Parker, 1976) with the exponential solution (29) using Euler's formula and the superposition principle for linear systems:

$$\chi(x,y) = \begin{cases} \cos(k_x x) \sin(k_y y) = \frac{1}{2} \Im \left\{ \exp[i(k_x x + k_y y)] + \exp[i(-k_x x + k_y y)] \right\} & \text{for odd } m \\ \sin(k_x x) \cos(k_y y) = \frac{1}{2} \Im \left\{ \exp[i(k_x x + k_y y)] + \exp[i(k_x x - k_y y)] \right\} & \text{for even } m \end{cases}$$
(32)

Figure 2 shows cases that are investigated in this work to determine the onset of the disturbances, namely: m=0 for perfect two-dimensional instabilities such as dunes, antidunes and roll waves spanning across the channel width (Charru et al., 2013; Bohorquez et al., 2019); m=1 for the alternate bars with a channel width of a quarter of the transverse wavelength, i.e., $\hat{\Lambda}_y=4\,\hat{B}$ (Nelson, 1990; Seminara, 2010); m=2 for the central mode developing an isolated train of three-dimensional antidunes (Kennedy, 1960; Yokokawa et al., 2010; Inoue et al., 2020); m=4 for double-row bars composed of a mid-channel bar and lateral bars (Parker, 1976; Rhoads, 2020); m=6 for double-train antidunes (Guy et al., 1966); m=14 for four-train roll waves over spillways (California Department of Water Resources: Galleries, 2025).

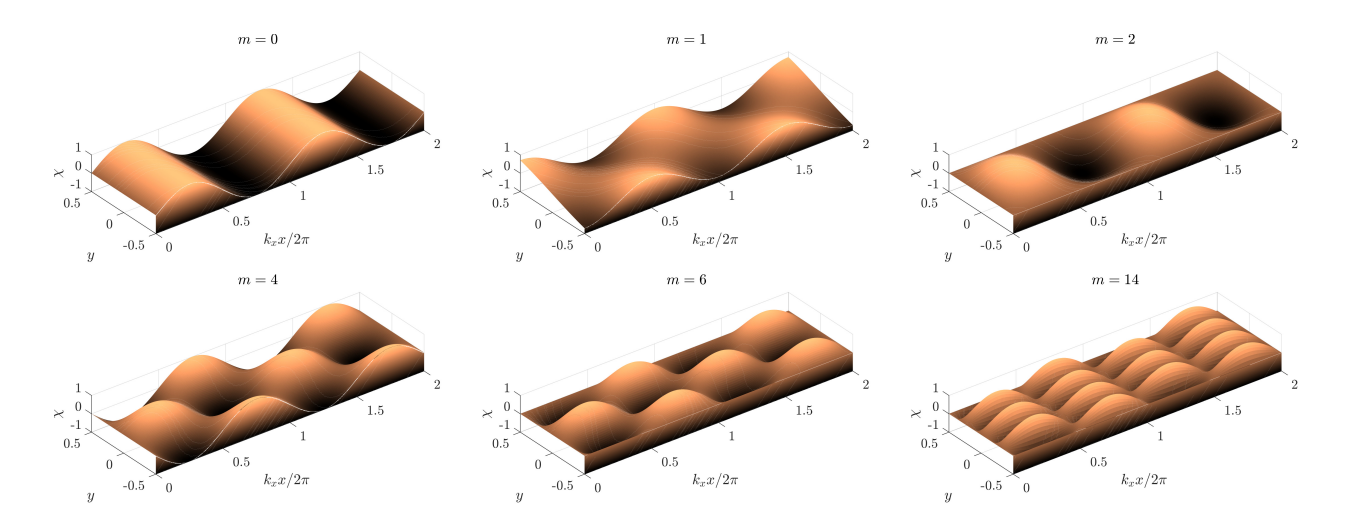


Fig. 2: Instability patterns $\chi(x,y)$ evaluated from Eq. (32) with different values of m.

Substituting Eq. (29) into the scaled governing equations (23)–(27) leads to the generalized eigenproblem, $\mathbf{M} \cdot \mathbf{T} = 0$, where the stability matrix \mathbf{M} is given by:

$$\mathbf{M} \equiv -\mathrm{i}\,\omega\,\mathbf{A} + \mathrm{i}\,k_x\,\mathbf{B} + \mathrm{i}\,\frac{\pi}{2}\,m\,\mathbf{C} + \frac{k_x^2}{\beta}\,\mathbf{D} + \frac{\pi^2}{4\,\beta}\,m^2\,\mathbf{E} + \beta\,\mathbf{F}\,,\tag{33}$$

with

$$\mathbf{A} \equiv \begin{pmatrix} 1 & 0 & 0 & 0 & 0 \\ 0 & \mathcal{F}r^2 & 0 & 0 & 0 \\ 0 & 0 & \mathcal{F}r^2 & 0 & 0 \\ 0 & 0 & 0 & 1 & 0 \\ 0 & 0 & 0 & 0 & 1 \end{pmatrix}, \quad \mathbf{B} \equiv \begin{pmatrix} 1 & 1 & 0 & 0 & 0 \\ 1 & \mathcal{F}r^2 & 0 & 0 & 1 \\ 0 & 0 & \mathcal{F}r^2 & 0 & 0 \\ 0 & a & 0 & a & 0 \\ 0 & 0 & 0 & 0 & 0 \end{pmatrix}, \quad \mathbf{C} \equiv \begin{pmatrix} 0 & 0 & 1 & 0 & 0 \\ 0 & 0 & 0 & 0 & 1 \\ 0 & 0 & a & 0 & 0 \\ 0 & 0 & 0 & 0 & 0 \end{pmatrix}, \quad \mathbf{F} \equiv \begin{pmatrix} 0 & 0 & 0 & 0 & 0 \\ -S & 2S & 0 & 0 & 0 \\ 0 & 0 & S & 0 & 0 \\ 0 & -\kappa_{\eta} \gamma'_{ss} & 0 & \kappa_{\eta} & 0 \\ 0 & \kappa_{\gamma} \gamma'_{ss} & 0 & -\kappa_{\gamma} & 0 \end{pmatrix}.$$

$$(34)$$

The solutions to the generalized eigenproblem are the eigenvector $\mathbf{T} \equiv (H_{\epsilon}, U_{\epsilon}, V_{\epsilon}, G_{\epsilon}, Z_{\epsilon})^T$ and the complex eigenvalue ω . The dispersion relation, which links the real longitudinal wavenumber k_x to the complex frequency ω and the lateral mode m was derived by setting the determinant of the stability matrix (33)–(34) to zero, i.e. $\mathbb{D}(k_x, \omega; m) \equiv |\mathbf{M}| = 0$. The base flow is unstable (stable, respectively) when the growth rate is positive $\omega_i > 0$ (negative $\omega_i < 0$, respectively). These solutions make it possible to obtain the neutral curve ($\omega_i = 0$), which determines the conditions for the growth of small amplitude instabilities.

The matrices **A** to **F** in Eq. (34) do not depend on the aspect ratio β and Fourier mode m because the parameters involved in their definitions are, or depend on, \mathcal{F}_{ℓ} and S (or d), as explained in § 2.3. The parametric dependence of the wavenumber k_x and frequency ω on m and β is given

by the stability matrix **M** (33). Our theory recovers the original result of Fredsøe (1978), who showed that the lateral mode m of multi-row bars could be identified by the change of variables $k_x = m k_{x1}$, $\omega = m \omega_1$ and $\beta = m \beta_1$ (Seminara et al., 2023). Therefore, the complex growth rate for mode m at $(m k_{x1}, m \beta_1)$ is equal to m times the growth rate of the first mode at (k_{x1}, β_1) :

$$\left[-i \,\omega_1 \,\mathbf{A} + i \,k_{x1} \,\mathbf{B} + i \,\frac{\pi}{2} \,\mathbf{C} + \frac{k_{x1}^2}{\beta_1} \,\mathbf{D} + \frac{\pi^2}{4 \,\beta_1} \,\mathbf{E} + \beta_1 \,\mathbf{F} \right] \cdot \mathbf{T} = 0.$$
 (35)

Our results apply not only to multiple-row bars but also to other instabilities of the mobile sediment bed (e.g., multi-train antidunes and three-dimensional antidunes) as well as the roll wave watersurface instability, opening the way for an explanation of their formation in a single theoretical framework.

We can comment on how bed and free-surface instabilities are related to each other in our model. Let H_{ϵ} and Z_{ϵ} be the first and last components of the eigenvector \mathbf{T} : H_{ϵ} is the free surface deformation amplitude, while Z_{ϵ} is the disturbance height of the bed. When solving the generalized eigenproblem (35) for **T**, we connect both free-surface deformation and bedform amplitude. This mathematical solution has a physical interpretation. Let us first assume that the mobile sediment bed starts being unstable, and therefore a bedform grows. The free surface responds to this change by forming a wave. For example, the two-dimensional antidune causes the water surface to adapt to bed evolution. If we now assume a free-surface instability such as roll waves over an erodible bed, the water surface disturbance reshapes the initially planar bed. As long as the height of the bedform and the amplitude of the disturbance are small, the interaction between them remains linear or weakly nonlinear. When it is no longer the case, more complex and nonlinear interactions occur between the water body, mobile sediment bed, and channel sidewalls. Typical examples include the supercritical flows that develop transverse and oblique jumps, provoking rooster-tails above two-dimensional antidunes (Kennedy, 1960; Robillard, 1965), roll waves over rhomboid bed pattern (Karcz and Kersey, 1980) and cyclic steps in open-channel flows (Balmforth and Vakil, 2012; Slootman and Cartigny, 2020). These nonlinear phenomena are outside the scope of linearstability theory.

3. Results

3.1. Roll waves in a clear water flow on a manmade flume

We will now show how the linear stability theory, introduced in Section 2.4, predicts the occurrence of the multi-train, alternate and single roll waves, as shown in Figure 3. On very rare occasions, flows in the main spillway of the Oroville Dam—the highest earth-fill dam in the United States—have shown spontaneous formation of multi-train roll waves. For instance, Fig. 3a taken on 31 January 2024 showed four parallel trains of roll waves. On 30 March 2011, alternate roll waves were observed for an even higher flow, as shown in Fig. 3b. At the same water discharge and date, single roll waves also formed at different times (Fig. 3c). The coexistence of alternate and single roll waves for the same flow parameters highlights the complexity of flow dynamics.

We focus on the Oroville Dam spillway, primarily due to the availability of discharge data (California Department of Water Resources: California Data Exchange Center) and historical photographs showing the reservoir spilling over time (California Department of Water Resources: Galleries, 2025). Furthermore, the large dimensions of the spillway allow for the identification of roll waves in satellite imagery. An aerial photograph shows the channel with several roll waves in August 1969, June 2011, May 2013, and July 2023 (Fig. 4). The Oroville Dam experienced spillway



Fig. 3: Photographs of the Oroville Dam's 931 m long and 54.5 m wide spillway in the United States (California Department of Water Resources: Galleries, 2025) show the development (a) multi-train roll waves at a discharge of 2000 cfs (56.6 m³·s⁻¹) on 31 January 31 2024, and (b) alternate and (c) one-dimensional roll waves observed on 30 March 2011, at a flow rate of 15 000 cfs (424 m³·s⁻¹). The estimated parameter values are (a) $\beta = 484$, $\ell = 2.7 \times 10^{-3}$ and $\ell = 8.8$ and (b)-(c) $\ell = 140$, $\ell = 7.9 \times 10^{-4}$ and $\ell = 10.3$. (d) A view of Brock's channel illustrates natural roll waves with $\ell = 22$, $\ell = 5 \times 10^{-3}$ and $\ell = 5.6$ (Negative No. 7842 in Brock, 1968). The flow direction is from top to bottom.

damage in February 2017, resulting in the evacuation of 188,000 residents downstream (Koskinas et al., 2020).. The Oroville spillway has a rectangular cross-section, measuring 54.5 m in width and 7 m in height (France et al., 2018; Koskinas et al., 2020). It includes a concrete-lined chute that descends from an elevation of 248.25 m down to a level just above the river bed at an elevation of 99 m. The structure is 931 m long and includes three distinct parts from top to bottom: (i) the inlet is straight, 274-m long with a slope of 5.66 %; (ii) the intermediate curved channel is 244-m long, with an elevation drop of 32.8 m; (iii) the outlet is 413-m long, with a slope of 24.5 %. We applied linear stability theory to the downstream part of the spillway, where the roll waves were

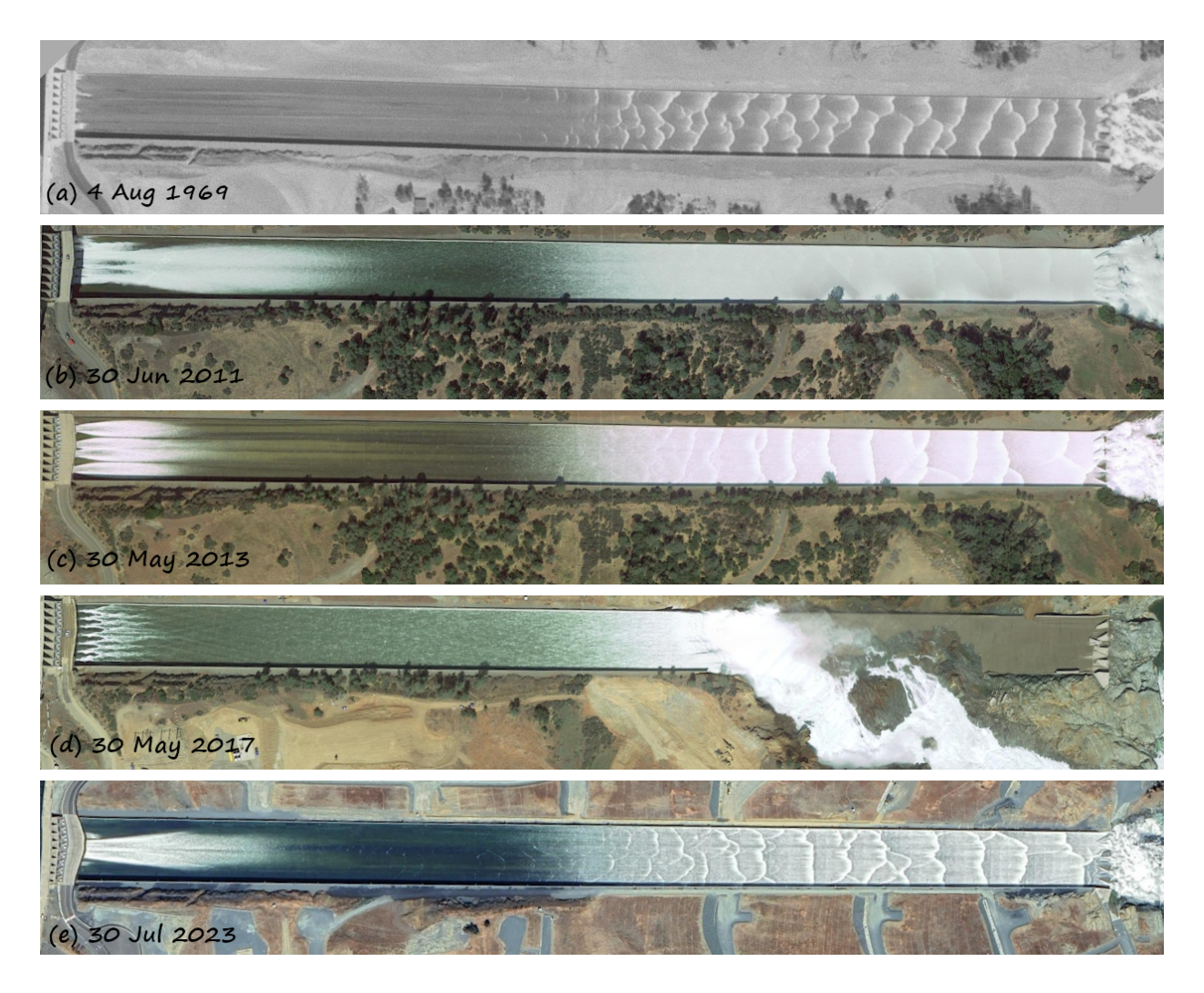


Fig. 4: Google Earth satellite images of the 931-m-long and 54.5-m-wide Oroville Dam spillway in the United States show the formation of roll waves with characteristic wavelengths in the nonlinear saturated regime of (a) 10-25 m in 1969, (b) 20-50 m in 2011, (c) 20-65 m in 2013 and (e) 25-60 m in 2023. Panel (d) shows the spillway structures crumbling in 2017. Flow from left to right.

photographed (see Figure 3) and observed by satellite (see Figure 4).

Table 1 shows the key variables including channel width \widehat{B} , bottom slope S, roll wave wavelength $\widehat{\Lambda}$, water flow rate \widehat{Q} and bed roughness \widehat{d} for the flows in panels a, b and c of Fig. 3, which are labelled as cases RW-A, RW-B and RW-C, respectively. In addition, Brock's experiment is labelled as the RW-D case study, and is shown in Figure 3d for the completeness of our study. Table 1 also presents the depth $\widehat{\eta}_0$ and the velocity \widehat{u}_0 of the uniform base flow calculated from Eq. (18) and from the friction coefficient f (17).

We calculated the key dimensionless parameters \mathcal{F}_{t} using Eq. (14), d using Eq. (15), β using Eq. (16) and k_{x} using Eq. (30), obtaining the complex frequency $\omega = \omega_{r} + \mathrm{i}\,\omega_{i}$ from the dispersion relation $|\mathbf{M}| = 0$. In the stability matrix \mathbf{M} (33), we varied the transverse mode m from 0 to 3. Additionally, to account for the fixed-bed condition inherent in the nonerodible spillway, we set $\kappa_{\eta} = \kappa_{\gamma} = 0$ in the submatrix \mathbf{F} (34). Table 2 shows the resulting dimensionless parameters and

Case	\widehat{B} (m)	S	$\widehat{\Lambda}_x$ (m)	$\widehat{Q} \; (\mathrm{m}^3 \cdot \mathrm{s}^{-1})$	\widehat{d} (mm)	$\widehat{\eta}_0$ (m)	$\widehat{u}_0 \; (\mathrm{m/s})$	f_0
RW-A	54.5	0.245	13.5 ± 4.5	56.6	0.305	0.11	9.44	0.025
RW-B	54.5	0.245	65.4	424	0.305	0.39	19.95	0.018
RW-C	54.5	0.245	32	424	0.305	0.39	19.95	0.018
RW-D	0.117	0.119	0.519	8×10^{-4}	0.027	5.3×10^{-3}	1.28	0.030

Table 1: Characteristic values for the case studies in Fig. 3.

the growth rates ω_i for each m-mode.

Case	β	\mathcal{F} r	$d \times 10^3$	k_x	$k \times 10^2$	$\omega_{i m=0}$	$\omega_{i m=1}$	$\omega_{i m=2}$	$\omega_{i m=3}$
RW-A	484	8.8	2.70	30 ± 10	5.76 ± 1.92	2.609 ± 0.5	2.607 ± 0.5	2.602 ± 0.5	2.594 ± 0.5
RW-B	140	10.3	0.79	5.2	3.75	0.553	0.546	0.529	0.501
RW-C	140	10.3	0.79	10.5	7.66	0.805	0.801	0.790	0.772
RW-D	22	5.6	5.04	1.42	6.45	0.107	0.072	0.026	-0.013

Table 2: Dimensionless parameters used to evaluate the growth rates ω_i in the dispersion equation for modes from m=0 to m=3 and the case studies in Fig. 3 and Table 1.

The series of experiments makes it possible to examine how the aspect ratio β affects the most unstable m-mode. It is worth noting that β is approximately 500 in the Oroville spillway under low water discharge (case RW-A, see Fig. 3a), which far exceeds the lowest β value studied, which was around 20 in Brock's experiment (case RW-D, see Fig. 3d). In addition, the other parameters are limited to narrower ranges, with $\mathcal{F}_{\mathcal{I}}$ between [5.6, 10.3], d in [0.79, 5.04], and k_x from [1.42, 40]. The scaled wavenumber based on the water depth, $k \equiv 2\pi \hat{\eta}_0/\hat{\Lambda}_x$, which is commonly used in roll waves studies (Jeffreys, 1925; Dressler, 1949), also shows a narrower range than its counterpart k_x , since we have $0.037 \le k \le 0.076$ for a wide range of Froude numbers.

Table 2 shows that the growth rates ω_i predicted by linear stability theory are increasingly sensitive to the m-mode as β decreases. Specifically, in case RW-A ($\beta \approx 484$), ω_i remains almost constant regardless of the value of m, whereas in case RW-D ($\beta = 22$), the growth rate becomes unstable for m = 0 (i.e., $\omega_i = 0.107$) and eventually stabilizes at m = 3 (i.e., $\omega_i = -0.013$). Cases RW-B and RW-C, with $\beta = 140$, serve as intermediate scenarios between RW-A and RW-D. The primary distinction between RW-B and RW-C lies in the wavenumber, which is $k_x = 5.2$ for case RW-B and $k_x = 10.5$ for case RW-C. In both cases, the effect of the transverse mode m on the growth rate ω_i is minimal, yielding approximate values of $\omega_i \approx 0.5$ for case RW-B and $\omega_i \approx 0.8$ for case RW-C.

In order to illustrate the influence of the aspect ratio β and the transverse mode m on the stability of the base flow, we plotted the neutral curve along with the contours of the growth rate ω_i in the $\{\mathcal{F}\iota, k_x\}$ -plane (for the values of β and m reported in Table 2) in Fig. 5. The neutral curves characterized by $\omega_i = 0$ are drawn as a thick continuous line, indicating the transition between the stable and unstable regions, and the constant growth rate curves are represented by a brown colour map. To compute ω_i in each panel, we set both β and ℓ to the specific values corresponding to cases A, B, C and D, while m was varied from 0 to 3. The first column in Figure 5 pertains to m = 0, the second column to m = 1, the third to m = 2, and the fourth to m = 3. Furthermore, the first row corresponds to the β and ℓ parameters in case RW-A, the second row pertains to cases RW-B and RW-C which share the same values, while the third row corresponds to case RW-D. Lastly, the symbols indicate the position of the wavenumber ℓ_x for the Froude number ℓ_x for each case study as follows: dark blue triangles for case RW-A, red cross and light blue cross for cases

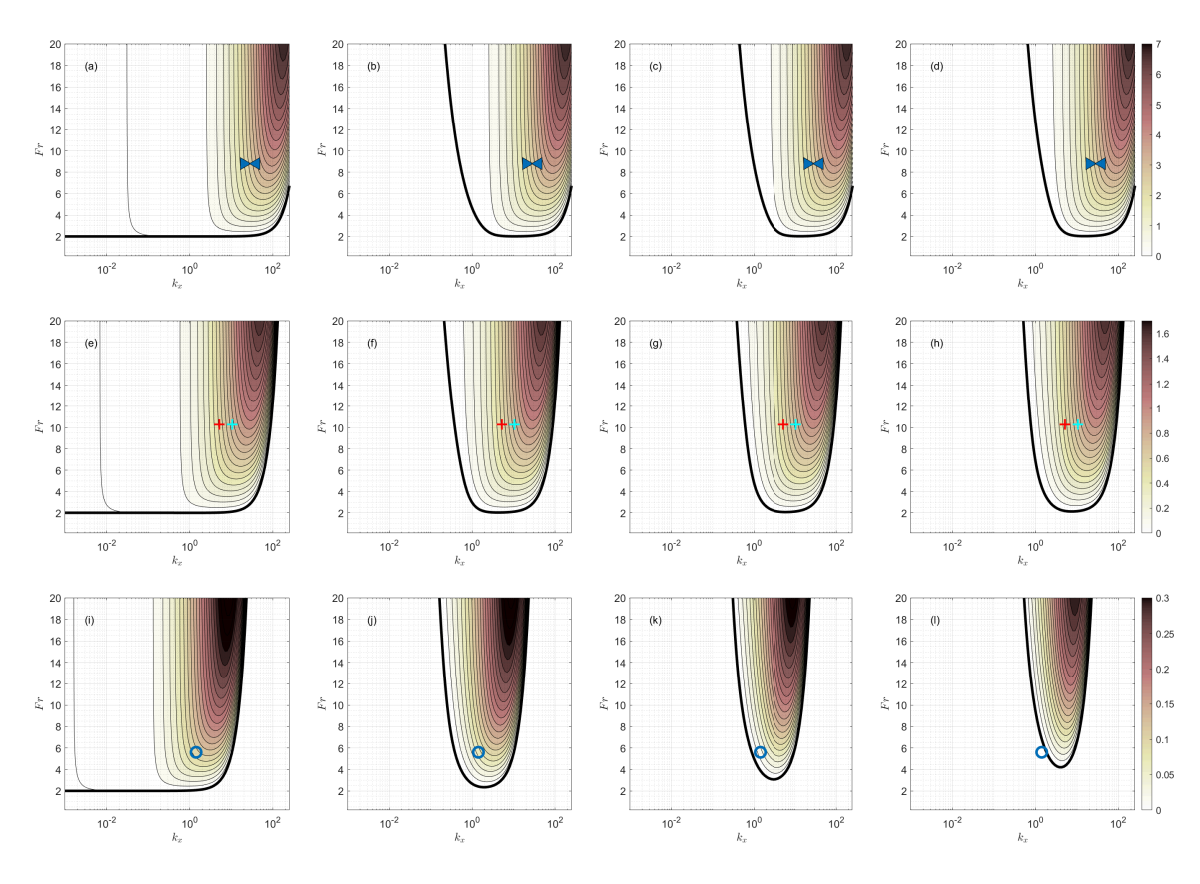


Fig. 5: Isocontours of the growth rate ω_i in the unstable region of the $\{\mathcal{F}\varepsilon,k_x\}$ -plane and neutral curve (thick solid line) related to roll wave instability of the free-surface flow. This is shown in (a)-(d) for $\{\beta=484, \ell=2.7\times 10^{-3}\}$, in (e)-(h) for $\{\beta=140, \ell=7.9\times 10^{-4}\}$, and in (f)-(l) for $\{\beta=22, \ell=5\times 10^{-3}\}$. Each column corresponds to: (a, e, f) the one-dimensional case m=0, (b, f, j) the alternate mode m=1, (c, g, k) the central mode m=2 and (d, h, l) the multi-train transverse mode m=3. The symbols indicate the corresponding cases in Fig. 3a with $\{\mathcal{F}\varepsilon=8.8, k_x=30\pm10\}$ (triangles in panels a-d), Fig. 3b with $\{\mathcal{F}\varepsilon=10.3, k_x=5.2\}$ (red cross in panels e-h), Fig. 3c with $\{\mathcal{F}\varepsilon=10.3, k_x=10.5\}$ (blue cross in panels e-h) and Fig. 3d with $\{\mathcal{F}\varepsilon=5.6, k_x=1.4\}$ (circle in panels i-l).

RW-B and RW-C, respectively, and blue circle for case RW-D.

As can be seen in Figs. 5a–d, for the lowest water discharge in the Oroville spillway (case RW-A), the growth rate contours tend to move closer together when the calculated wavenumber approaches the observed wavenumber (indicated by blue triangles) whatever the value of the mode number m. The main difference between the four figures is the appearance of the neutral curve (thick solid line) for m=0 (Fig. 5a) compared to $m=1\dots 3$ (Figs. 5c-d). Specifically, the m=0 curve develops a horizontal asymptote at $\mathcal{F}z=2$ for low wavenumbers. The stability criterion $\mathcal{F}z=2$ for m=0 corresponds to the classic criterion for the long traveling-wave solution of a single roll wave (see, for instance, Jeffreys, 1925; Dressler, 1949; Hwang and Chang, 1987; Yu and Kevorkian, 2000; Chang et al., 2000). In contrast, at high wavenumbers, turbulent viscosity stabilizes the base flow by introducing a cutoff in the wavenumber spectrum, which increases the critical value of the Froude number required for instability. This behavior corroborates the findings of previous studies that employed similar closure relations for turbulent stresses in the momentum balance equation (e.g., Needham and Merkin, 1984; Balmforth and Vakil, 2012; Bohorquez and Ancey, 2015). The

horizontal asymptote $\mathcal{F}_{\ell} = 2$ is absent from the neutral curves for higher-order modes m = 1 (Fig. 5b), m = 2 (Fig. 5c), and m = 3 (Fig. 5d), which lead to a U-shape. Consequently, low wavenumbers are stable for $m \geq 1$. The minimum value of \mathcal{F}_{ℓ} required for the growth of roll waves with $m \geq 1$ remains close to the critical value for m = 0 (i.e., $\mathcal{F}_{\ell} = 2$) in this case study. Furthermore, at the observed wavenumber $k_x = 30 \pm 10$ and for the base flow Froude number $\mathcal{F}_{\ell} = 8.8$, the value of m has a negligible effect on the growth rate contours. These conclusions also apply to the four trains of roll waves shown in Fig. 3a, which correspond to m = 14 (recall Fig. 2) and yield a growth rate of $\omega_i = 2.32$. Therefore, we conclude that the single, alternate, central, and multi-row roll waves are equally unstable.

The increase in water discharge in the Oroville spillway from $\widehat{Q}=56.6~\mathrm{m}^3\cdot\mathrm{s}^{-1}$ (case RW-A in Figs. 5a-d) to $\widehat{Q}=424~\mathrm{m}^3\cdot\mathrm{s}^{-1}$ (cases RW-B and RW-C in Figs. 5e-h) does not alter the qualitative observations described earlier. The most significant effect of reducing β from 484 (case RW-A) to 140 (cases RW-B and RW-C) is the shift of the neutral curves toward lower wavenumbers. The critical Froude number necessary for roll wave development remains at $\mathcal{F}\iota=2$, regardless of the m-mode. The wavenumbers estimated from the photographs in Fig. 3b ($k_x=5.2$) and Fig. 3c ($k_x=10.5$) at a Froude number of $\mathcal{F}\iota=10.3$ are indicated by the red and light blue crosses in Fig. 5 and are positioned close to the contour line of maximum growth rate. It is noteworthy that these wavenumbers are localized with precision in all transverse modes in the unstable region. As demonstrated in case RW-A, linear stability theory predicts that the three modes $0 \le m \le 3$ are unstable. These findings support the coexistence of alternate (m=1) and single roll waves along the Oroville spillway for the same base flow parameters, as shown in Fig. 3b and Fig. 3c, respectively.

Interestingly, Brock's experiment tells us another story. The parameter $\beta=22$ decreases significantly compared to the Oroville's cases, which shifts the neutral curves toward lower wavenumbers. In addition, for the transverse modes where $m\geq 1$, the U-shaped neutral curves become narrower, and the critical Froude number increases to 2.35 for m=1 (Fig. 5j), 3.07 for m=2 (Fig. 5k), and 4.2 for m=3 (Fig. 5l). These values are greater than the standard Froude number of $\mathcal{F}\iota=2$ for the single roll wave (m=0, Fig. 5i). It is important to note that the changes in the neutral curves cause the observed wavenumber $k_x=1.42$ at $\mathcal{F}\iota=5.6$ (indicated by the circle in Figs. 5i-l) in Brock's experiment (Fig. 3d) to become less unstable as m increases, and ultimately to become stable for m=3 (Fig. 5l). The highest growth rate, $\omega_i=0.107$, is achieved for m=0, which corresponds to the one-dimensional roll wave extending across the entire channel width (shown in Fig. 3b). The alternate mode (m=1) and the central mode (m=2) are also unstable but exhibit lower growth rates of $\omega_i=0.072$ and 0.026, respectively. This finding explains why Brock observed single roll waves: the m=0 mode is the most unstable in his experimental setup. Therefore, we conclude that Brock's flume was too narrow to allow for the formation of multi-train wave patterns, which are observed in much wider channels.

As a final note for this section, we must return to the question of why the roll waves at Oroville sometimes appear as multi-train patterns, while alternating and single roll waves appear at other times. The research conducted by Brock (1969, 1970) demonstrated that roll wave instability is significantly influenced by the hydraulic conditions at the flume inlet. For example, Brock was able to create steady periodic wave trains by oscillating a paddle in the entrance box of the channel at regular time intervals. In the Oroville spillway, disturbances originate from the seven gates controlling the flow discharge from Oroville Lake. The various flow patterns in the inlet area are visible in the aerial views of the spillway. For instance, Figures 4b and 4e show a single jet spanning



Fig. 6: Public domain photographs (California Department of Water Resources: Galleries, 2025) show (a) the Lake Oroville Main Spillway gates that control water releases and (b)-(d) the flow over the spillway. The photographs were taken during the following discharge events: (b) 4000 cfs (113 $\mathrm{m}^3 \cdot \mathrm{s}^{-1}$) on March 10, 2023; (c) 25 000 cfs (707 $\mathrm{m}^3 \cdot \mathrm{s}^{-1}$) on April 17, 2019; and (d) 160 000 cfs (4530 $\mathrm{m}^3 \cdot \mathrm{s}^{-1}$) on January 2, 1997.

almost the entire width of the channel. By contrast, Figures 4c and 4d show three and seven jets near the gates, respectively. This variation in the number of jets is even more evident in the on-site photographs of the seven gates of the Oroville main spillway (Fig. 6a), which illustrate the flow control along the downstream section of the spillway for water discharges from $100 \text{ m}^3 \cdot \text{s}^{-1}$ (Fig. 6b) to $4500 \text{ m}^3 \cdot \text{s}^{-1}$ (Fig. 6d).

In addition to the physical explanation given above, theoretical arguments indicate that the physical mechanism disturbing the flow determines the growing mode when all the *m*-modes are unstable (e.g., cases RW-A to RW-C). This is the case for *convective* instability, as demonstrated by Schmid and Henningson (2001). A system which is convectively unstable responds to localized disturbances that are swept away from the origin in the flow direction. In the case of convective instability, the flow will relax and return to its original state at any location if the source of the disturbance stops and the disturbance is advected downstream. The convective nature of the roll wave instability is well established. Indeed, the group velocity arising in the spatio-temporal linear stability analysis has been shown to be positive (Bohorquez, 2010); a similar conclusion is reached when using the impulse response or the Green function (Di Cristo and Vacca, 2005). We can therefore conclude that the disturbed flow downstream of the seven gates of the Oroville spillway defines the growing mode in case studies RW-A to RW-C.

3.2. Antidunes, multi-row antidunes or three-dimensional antidunes?

The photograph in Figure 7a, which corresponds to experiment 12 in Simons et al. (1963), displays a classic two-dimensional antidune formed within the sediment layer in a narrow channel, migrating upstream in the upper-flow regime. Above the antidune, surface water waves appear with a shape that is either periodic or nearly so. Kennedy (1960) called these waves stationary free-surface waves because they move very slowly, if at all, and remain in phase with the antidune. Assuming that the antidune retains its shape across the entire channel width, as shown in the image, Anderson (1953) and Kennedy (1963) applied potential flow theory to describe the two-dimensional water motion. They identified two key dimensionless parameters that control the growth of antidunes on erodible beds: the Froude number \mathcal{F}_{ℓ} , and the dimensionless wavenumber based on water depth

$$k \equiv 2\pi \frac{\widehat{\eta}_0}{\widehat{\Lambda}_x} \,. \tag{36}$$

Simons et al. (1963) also observed that bed features could have more complex structures, with the formation of double-train antidunes, when the channel width increased. The typical water-surface wave pattern above a double-train antidunes generally formed in two parallel lines of waves, as

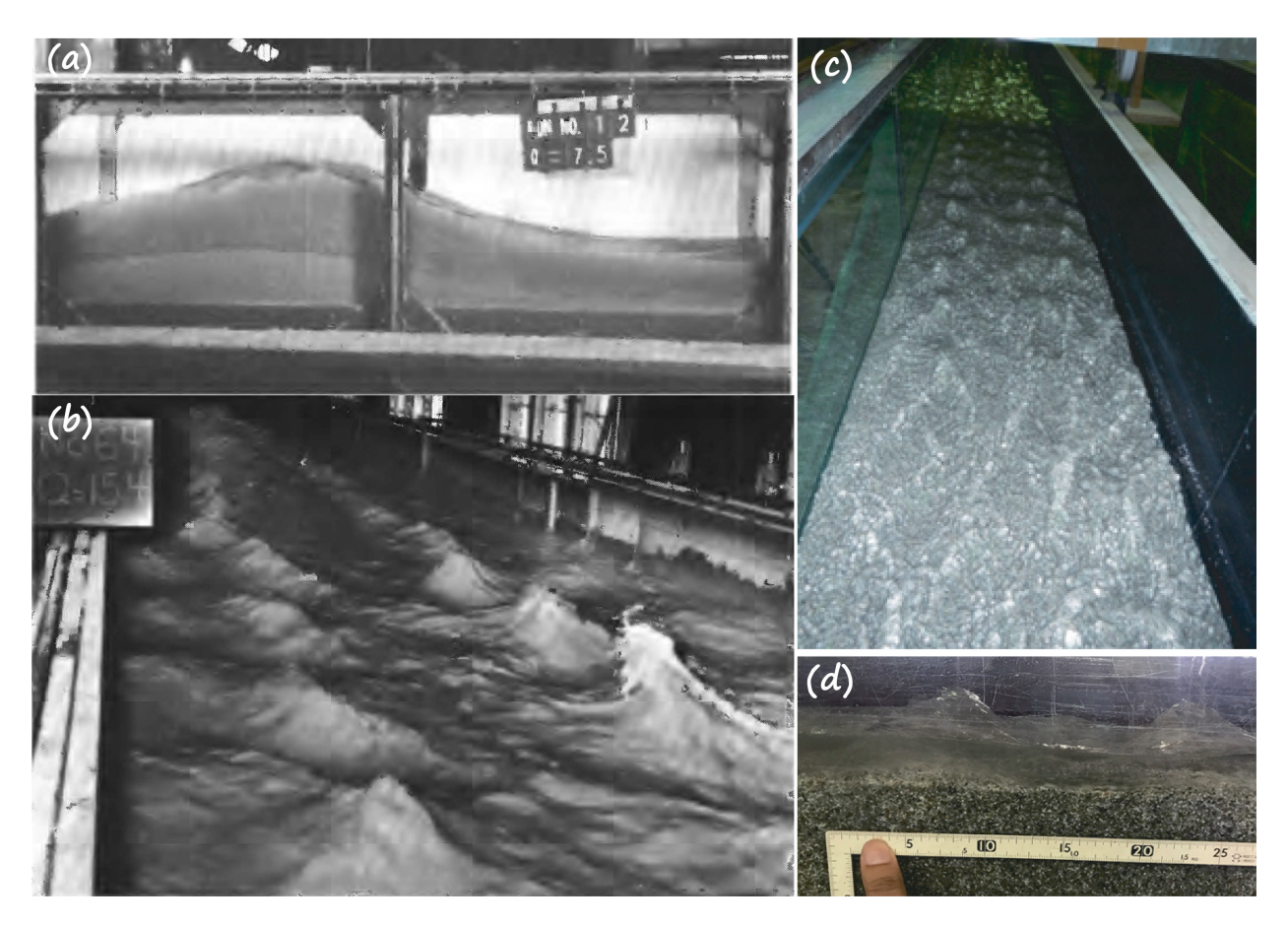


Fig. 7: (a) Case study AD-A: a lateral perspective of a stationary free-surface wave above a two-dimensional antidune, m=0 (refer to Fig. 16 in Simons et al., 1963). (b) Case study AD-B: a view from the upstream of the water-surface waves formed above a double-train antidunes, m=6 (refer to Fig. 97 in Guy et al. (1966)). (c) An illustration of triple-train antidunes (case study AD-C), m=10, transitioning into (d) a singular three-dimensional antidune (case study AD-D), m=2, at a later stage in Run 3 documented by Inoue et al. (2020) (see Figs. 7d and g, respectively, in Inoue et al. (2020)). The water-surface wave in the panel (d) shows a typical rooster-tail. Photographs (a)–(b) courtesy of the U.S. Geological Survey.

shown in Figure 7b. In this case, the surface water waves in each row were three-dimensional, likely the rooster tails described by Kennedy (1960) and had different characteristics and dynamics than when only a single train of antidune waves formed (p. G35 in Simons et al., 1963). More recently, Yokokawa et al. (2010) observed a cyclic transformation of two-dimensional antidunes into three-dimensional antidunes. In their Run 3, Inoue et al. (2020) observed the early formation of triple-train antidunes (see Fig. 7c), and later, the nonlinear evolution of these trains and their coalescence into a single three-dimensional antidune (see Fig. 7d).

In this section, we analyze the experiments shown in Fig. 7a and Figs. 7b—d to evaluate how well our linear stability theory can predict the formation of a single train of two-dimensional antidunes in a narrow flume and multiple trains of antidunes in wide channels, respectively. These experiments are referred to as case studies AD-A (Fig. 7a), AD-B (Fig. 7b), AD-C (Fig. 7c) and AD-D (Fig. 7d). In our approach, the aspect ratio β defined by Eq. (16) appears explicitly in the stability matrix **M** [see Eq. (34)] and implicitly in the definition of the dimensionless wavenumber

 k_x in Eq. (30), which is related to the Kennedy wavenumber k (36) by the following relationship:

$$k_x = \beta k. (37)$$

Table 3 summarizes the main variables and dimensionless parameters for each experiment. All experiments have similar Froude numbers $(1.3 \le Fr \le 1.39)$ and wavenumbers $(0.58 \le k \le 0.81)$. The main differences are the following: (i) the aspect ratio β is significantly smaller in AD-A $(\beta \approx 3)$ than in AD-B to AD-D $(\beta \approx 20)$; (ii) the relative roughness is considerably coarser in AD-C and AD-D $(d \approx 0.06)$ than in AD-A and AD-B $(d \approx 0.003)$.

Case	\hat{B} (m)	$\widehat{Q} \; (\mathrm{m}^3 \cdot \mathrm{s}^{-1})$	S	$\widehat{\Lambda}_x$ (m)	\widehat{d} (mm)	$\widehat{\eta}_0$ (m)	f_0	β	$\mathcal{F}r$	$d \times 10^3$	k_x	k
AD-A	0.61	0.222	0.0144	2.13	0.56	0.195	0.063	3.12	1.39	2.9	1.79	0.58
AD-B	2.44	0.442	0.0578	1.04	0.49	0.125	0.027	19.5	1.31	3.9	14.78	0.76
AD-C	0.5	0.008	0.0145	0.193	1.42	0.025	0.068	20	1.30	56.8	16.28	0.81
AD-D	0.5	0.008	0.0145	0.247	1.42	0.025	0.068	20	1.30	56.8	12.72	0.64

Table 3: Characteristic values for the case studies corresponding to Run 12 in Simons et al. (1963) (case AD-A, Fig. 7a), Run 64 in Guy et al. (1966) (case AD-B, Fig. 7b) and Run 3 in Inoue et al. (2020) at the early stage (case AD-C, Fig. 7c) and after 30 minutes (case AD-D, Fig. 7d).

Before examining our model's predictive capabilities, we have drawn in Fig. 8a the regions of the $\{\mathcal{F}_{\mathcal{F}}, k\}$ -plane (colored in light purple) where some of the existing linear-stability analyses predict the growth of two-dimensional antidunes (Anderson, 1953; Kennedy, 1969; Charru et al., 2013). We have also included the same dataset on antidunes as in our previous works (Bohorquez and Ancey, 2015; Bohorquez et al., 2019), shown by the dots in Fig. 8. Kennedy's (1969) linear stability theory predicts the growth of antidunes for $\Im \iota \ge \Im \iota_{cr,1} = k^{-1/2} \tanh^{1/2} k$, and thereby improves the predictions of the potential flow theory developed by Anderson (1953), who set the critical Froude number to $\mathcal{F}_{cr,2} = \left[\sinh 2k/k \left(\tanh k \sinh 2k - 2\right)\right]^{1/2}$. More complex theories have employed a rotational two-dimensional flow model that constrains further the region of the $\{\mathcal{F}_{\ell}, k\}$ -plane where antidunes can develop (e.g., Bose and Dey, 2009; Camporeale and Ridolfi, 2011; Andreotti et al., 2012; Charru et al., 2013). The purple area in Fig. 8a is in agreement with available experimental data (green dots). Similarly, Figures 8b and 8c show the conditions required by the governing equations (10)–(13) to observe the development of two-dimensional antidunes in the plane $\{k, \mathcal{F}r\}$ and the three-dimensional parameter space $\{k, \mathcal{A}, \mathcal{F}r\}$, respectively. These conditions were obtained simply by setting $\beta = 1$ (i.e., $k = k_x$) and m = 0 (i.e., $k_y = 0$) in the eigenproblem M (33). Varying the dimensionless parameters in the same range of parameters as in the antidune dataset (i.e., $10^{-3} \le \ell \le 0.6$ and $0.7 \le \mathcal{F}_{\ell} \le 2.3$) yields the bed instability region for the antidunes (green area in Fig. 8b and above the gree surface in Fig. 8c). We have marked the case studies AD-A (blue rhomboid), AD-B (yellow cross), AD-C (magenta triangle) and AD-D (red circle) with distinctive symbols. The one-dimensional version of our theory predicts that the four case studies satisfy the conditions required to form a two-dimensional antidune. Moreover, this conclusion applies to the entire dune-antidune database. The current method recovers our previous results (Bohorquez et al., 2019), which can therefore be considered a special case of the more general theory (33)–(34) with m=0.

For completeness, we extended the calculations beyond the maximum Froude number of antidune experiments (i.e., $\Im z \ge 2.3$) and analyzed all the unstable eigenvalues in the eigenproblem **M** (33). Apart from the antidune bed instability, we identified a second instability originating from the free surface, which triggers roll waves at $Fr \ge 2$. Figure 8b shows in blue the unstable region

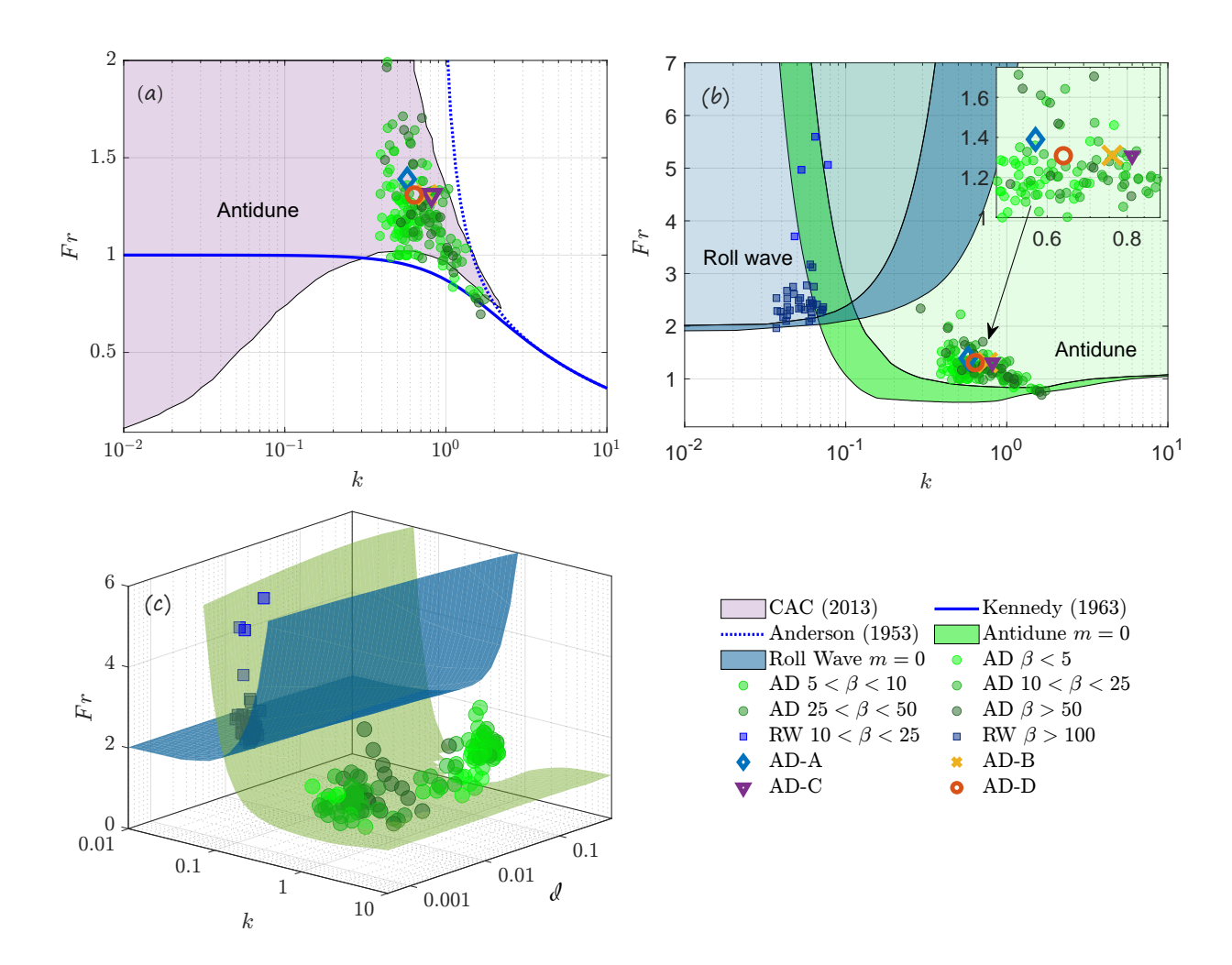


Fig. 8: (a) Classic representation in the parameter space $\{k, \mathcal{F}\iota\}$ of the regions of bed instability for pure twodimensional antidunes, as obtained by Anderson (1953), Kennedy (1969) and Charru et al. (2013). (b) Regions of bed instability (green area) and free-surface flow instability (blue area) where antidunes and roll waves form, respectively, according to the current theory with $\beta=1$ (i.e., $k=k_x$) and m=0 (i.e., $k_y=0$) in the eigenproblem \mathbf{M} (33). Panel (b) is the projection of the three-dimensional space $\{k, \mathcal{J}, \mathcal{F}\iota\}$ shown in panel (c) onto the twodimensional plane $\{k, \mathcal{F}\iota\}$. Our theory in (b)-(c) accounts for the relative roughness, which varies as in the antidune dataset (Bohorquez and Ancey, 2015; Bohorquez et al., 2019) represented with green dots (i.e., $10^{-3} \leq \mathcal{J} \leq 0.5$). Panels (b)-(c) also show the dataset of roll waves by Brock (1969) and Zhao et al. (2015) with the square symbols in blue. Case studies of antidunes AD-A (Fig. 8a), AD-B (Fig. 8b) and AD-C, D (Fig. 8c,d) are marked with a blue rhomboid, yellow ×-symbol, magenta triangle and red circle, respectively.

where roll waves can develop even when the bed is erodible (i.e., actual results with $\kappa_{\gamma} \neq 0$ and $\kappa_{\eta} \neq 0$) instead of fixed (as in Section 3.1). Additionally, Figure 8c displays the critical surface for the roll wave. The experimental dataset of antidunes lies below this critical surface (i.e., within the free-surface stable region), indicating that both instabilities are unrelated. Therefore, an important contribution of our theory is its ability to capture not only bed instabilities but also (independent) free-surface flow instabilities.

We have to add a note of caution regarding the interpretation of Figure 8. First, most authors did not distinguish between the different types of antidune (two- or three-dimensional antidunes,

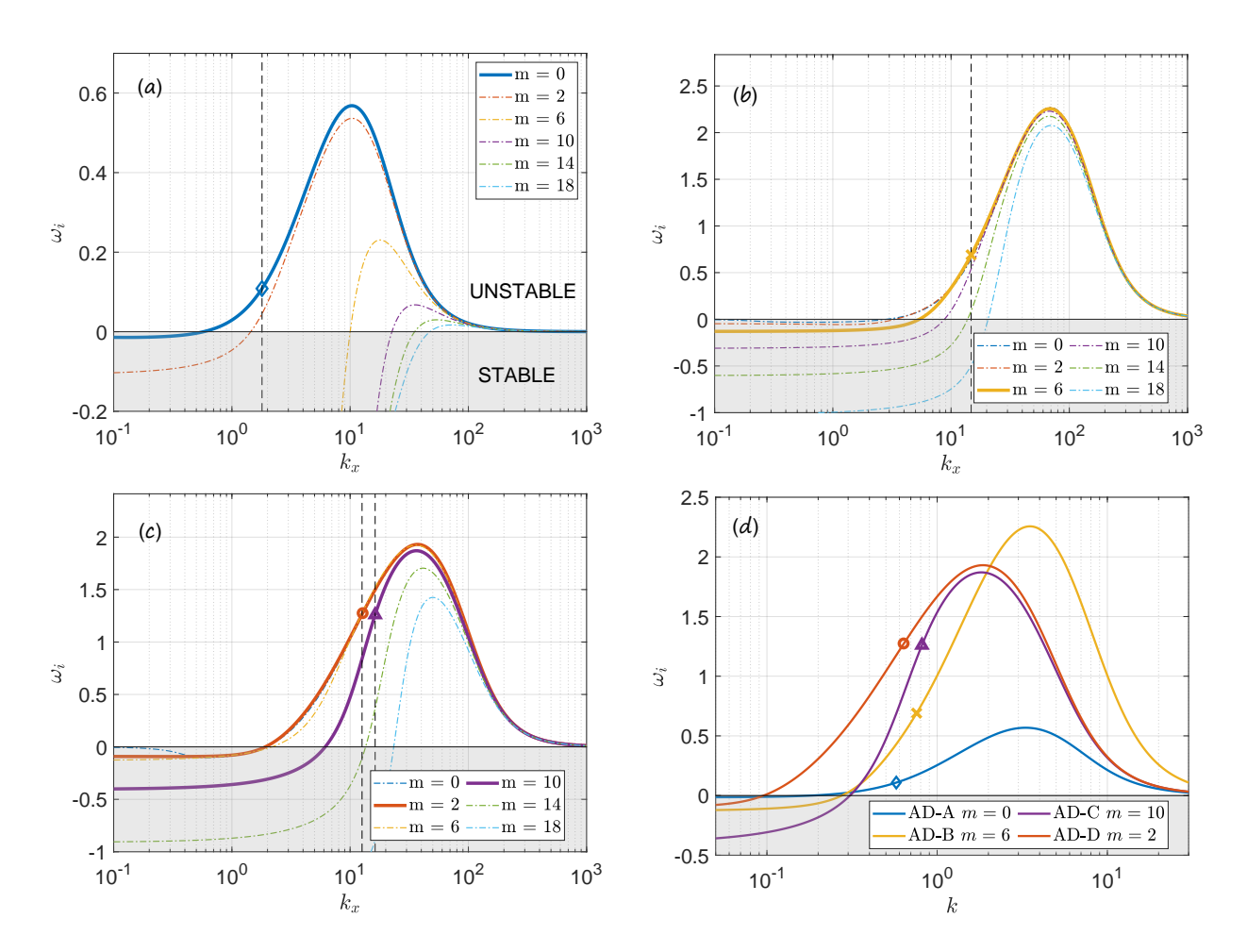


Fig. 9: Growth rates ω_i of the antidune eigenvalue as a function of the wavenumber k_x (30) and the transverse mode m for case studies (a) AD-A (Fig. 7a), (b) AD-B (Fig. 7b) and (c) AD-C,D (Fig. 7c,d). The curves of the mode observed in the experiments are highlighted with a thick solid line, and the vertical dashed line gives the wavenumbers measured in the flume. Panel (d) summarises the results of the four case studies using the classic nondimensional wavenumber $k = k_x/\beta$ (37).

single or multiple rows) and used the whole set of experimental data as if they were two-dimensional. Second, most theorists have so far overlooked the flow dynamics in the cross-stream direction, which severely limits the modeling capability of three-dimensional or multi-row antidunes. Our linear stability analysis in Eqs. (33)–(34) overcomes this limitation by providing predictions of multi-row instabilities in agreement with experimental observations (see Fig. 7). We will now go into detail on this last point.

To assess the consistency of the proposed theory, we compared the wavenumber and the antidune typology of each case study by setting the aspect ratio β , the Froude number $\mathcal{F}\iota$, the bed slope S, and the relative grain roughness ℓ to the experimental values reported in Table 3. To improve accuracy of our prediction, we calibrated the base-flow friction factor f_0 from laboratory experiments by using the equation $f_0 = 8 S/\mathcal{F}\iota^2$. We then solved the generalized eigenproblem (33)–(34) to find the growth rate ω_i as a function of the wavenumber k_x for plausible physical configurations of the antidunes. We examined two-dimensional (m = 0), three-dimensional (m = 2),

double-row (m = 6), triple-row (m = 10), quadruple-row (m = 14), and quintuple-row (m = 18) antidunes. Results are summarized in Fig. 9a and Fig. 9b for Run 12 (Fig. 7a) and Run 64 (Fig. 7b) by Simons et al. (1963), and Fig. 9c for Run 3 (Figs. 7c-d) by Inoue et al. (2020).

For the two-dimensional antidune reported by Simons et al. (1963) (i.e., case AD-A), the widest range of unstable wavenumbers is obtained by selecting the two-dimensional mode m=0 (thick blue line in Fig. 9a). At the specific wavenumber $k_x = 1.8$ observed in the flume (see Fig. 7a), marked with a vertical dashed line in Fig. 9a, the growth rate reaches the positive value $\omega_i = 0.108$ for m=0, decreases to $\omega_i=0.05$ for the three-dimensional mode (m=2) and becomes negative for $m \geq 6$, which prevents the formation of multi-row antidunes. In the double-train antidunes observed by Simons et al. (1963) (i.e., case AD-B), the theory also agrees with the flume experiment shown in Fig. 7b with $k_x = 14.78$. The growth rate at this wavenumber reaches the maximum value (i.e., $\omega_i = 0.69$) for the mode m = 6 (thick yellow curve in Fig. 9b) that corresponds exactly to the double-train antidune. The growth rates for the two-dimensional antidune (m=0, dasheddotted line in blue) and the three-dimensional antidune (m=2, dashed-dotted line in red) are slightly lower. The mode m=6 is therefore more unstable than the modes m=0 and m=2, and this higher instability explains the development of the double-row antidune in the flume instead of a two-dimensional or three-dimensional antidune. In the third study case, Inoue et al. (2020) reported the formation of triple-row antidunes (Fig. 7c) and three-dimensional antidunes (Fig. 7d). The growth-rate curves correspond, respectively, to the magenta (m=10) and red (m=2) solid lines in Fig. 9c. Our theory predicts that the wavenumbers observed in the experiments are unstable with growth rates of $\omega_i = 1.25$ at $k_x = 12.7$ for m = 2 and $\omega_i = 1.26$ at $k_x = 16.3$ for m = 10. The higher order transverse mode m = 14 (dashed-dotted line in green) is less unstable ($\omega_i < 0.5$) and, in the case of m=18 (dashed-dotted line in blue), it becomes stable. The greater growth rate for m=2 than for m=10 explains why the antidune in Run 3 (Inoue et al., 2020) was, at later times, three-dimensional (case AD-D) instead of multi-row (case AD-C). Alternate bars also formed in the same experiment, as predicted by our theory in Section 3.3.

Figure 9d compares the growth rate curves $\omega_i(k)$ of the three experiments using the classic wavenumber definition $k = k_x/\beta$ in Eq. (37) proposed by Anderson (1953) and Kennedy (1963). The wavenumbers are marked with the same symbols as in Kennedy's diagram (see Fig. 8b), showing that the four pairs of values k- $\mathcal{F}\iota$ nearly overlap. However, the topology of the antidune differed in each flume experiment (see Fig. 7), underscoring the role of dimensionless parameters such as d, β and m in characterizing the bedform regime. Our theory accounts for the additional parameters affecting the growth rate ω_i as illustrated in Fig. 9d.

3.3. Alternate bars and multiple bars

This section first demonstrates that, from a linear stability perspective, non-capacity bedload transport equations can also predict alternate bar formation. Second, it demonstrates that, within our theoretical framework, the same flow conditions can generate other bedforms such as antidunes and rhomboidal bars, which can even coexist with alternate bars. To this end, we have selected four case studies (see Table 4) with β values representative of the conditions under which alternate bars have been observed experimentally (Cheng and da Silva, 2023): case AB-A corresponds to Run-63 in Jaeggi (1984) with $\beta = 8.1$; case AB-B is Run 2 in Moteki et al. (2023), with $\beta = 16.38$, where free-surface disturbances, rhomboid bars and alternate sandbars form at different stages; case AB-C is Run 3 in Inoue et al. (2020), with $\beta = 20$, in which triple-row and three-dimensional antidunes (already analyzed as cases AD-C and AD-D in Section 3.2) coexist with alternate bars;

finally, case AB-D is Run 80 in Ikeda (1983), with $\beta = 38.46$, where rhomboid bars, antidunes and alternate bars formed on a fine gravel bed over time.

Case	AB-A	A	В-В	A	B-C	Al	B-D		MI	3-A			$\mathrm{MB} ext{-}\mathrm{B}$	
\widehat{B} (m)	0.3	0.45		0.5		4		3.01				1.80		
\widehat{L} (m)	25	12		25		160		43				15		
\widehat{Q} (l/s)	6.1	2.57		8.1		402		30.20				4.00		
$\hat{\eta}_0$ (cm)	3.72	1.4		2.5		10.4		2.58			0.82			
\hat{d} (mm)	4	(.75	1.42		6		0.88			1.05			
S	0.0128	(C	.01	0.0145		0.0104		1/200				1/100		
$\mathcal{F}r$	0.9		1.1	1.3		0.96		0.79				0.97		
d	0.107	0.	.075	0.057		0.	058		0.0)34		0.112		
β	8.1	1	6.38		20	38	3.46		11	6.7		219		
m	1	1	10	1	10	1	16	4	8	12	16	4	8	12
Form	AB	AB	AD	AB	AD	AB	AD	MB	MB	MB	MB	MB	MB	MB
$\widehat{\Lambda}_x$ (m)	7.8	4	0.1	6	0.1	35	1.25	12.5	7.0	4.5	3.0	5.5	3.6	2.5
k_x	0.24	0.71	28.27	0.52	31.41	0.72	20.11	1.5	2.7	4.2	6.3	2.1	3.1	4.5
$k \times 10^2$	2.9	4.3	172.61	2.62	157.08	1.87	52.28	0.79	1.42	2.21	3.31	0.94	1.43	2.06

Table 4: Experimental conditions and characteristic values for the selected case studies Run-63 by Jaeggi (1984) (case AB-A), Run 2 by Moteki et al. (2023) (case AB-B), Run 3 of Inoue et al. (2020) (case AB-C) with the same flow conditions as former cases AD-C and AD-D in Section 3.2, Run 80 of Ikeda (1983) (case AB-D), and Runs B4 and C8 by Fujita (1989) (cases MB-A and MB-B, respectively).

To remain consistent with previous linear stability analyses based on the Exner equation, we used the wavenumbers that were derived for the alternate bars with m=1 from the measured length in the flow direction at late times, when the alternate bars were fully developed. Additionally, we identified the longitudinal wavenumbers of the higher-order transverse modes observed along the experimental run in cases AD-B, AD-C and AD-D. We evaluated the transverse mode as $m=4\widehat{B}/\widehat{\Lambda}_y$ (31) using the cross-section wavelength $\widehat{\Lambda}_y$ given in the literature or visible in the available data. In doing so, we can discuss from a theoretical viewpoint the part played by the short wavelengths in the development of alternate bars of longer wavelengths, as Seki et al. (2023) investigated experimentally. The values are given in Table 4. Here are the procedures: for case AB-B, we obtained the alternate bar length at $\hat{t} = 60$ min (Fig. 10g) and the higher wavenumbers for the early stage of the experiment at $\hat{t} = 2 \text{ min (Fig. 10d)}$ from the bed elevation contours; for case AB-C, the bedform parameters correspond to the bed elevation contour (Fig. 10b) and the photograph (Fig. 10c), reproduced from Inoue et al. (2020), with the flow turned off; for case AB-D, the wavelength and transverse mode at onset and fully-development stages were measured in the plan view of Figure 3-28 in Ikeda (1983) that yields four-row bars with m=16 at $\hat{t}=7$ min (Fig. 1d) and alternate bars with m=1 at $\hat{t}=73$ min (Fig. 1c). Lastly, the theoretical results were obtained by solving the generalized eigenproblem (33)–(34) for the aspect ratio β , Froude number \mathcal{F}_{ℓ} , bed slope S and relative grain roughness ℓ as in the experiments; the base-flow friction factor f_0 was given by $f_0 = 8 S/\Im r^2$ as in the antidune case (Section 3.2).

Figure 10 recaps our theoretical results and includes contour plots of the bed elevation for some of the studied cases illustrating the coexistence of alternate bars and bedforms with shorter wavelengths characteristic of antidunes. Figure 10a reports the growth rate curves $\omega_i(k_x)$ of the bar eigenvalue for the alternate mode m=1 as a solid line and the antidune eigenvalue as a dashed line. In addition, the symbols indicate the wavenumbers of the bedforms measured in the

experiments (see Table 4) for alternated bars (filled squares) and shorter bedforms (dots). Overall, there is a good agreement between theory and experiments. The measured wavenumbers lie within the instability range ($\omega_i > 0$) and are close to the maximum of the growth rate curves. Our theory predicts that the alternate bar wavelengths must be longer than a critical value for being unstable and growing over time in the experiment. The minimum streamwise length of the alternate bars for the studied cases, predicted by our linear-stability theory, is $\hat{\Lambda}_x = 2.4$ (AB-A), 3.3 (AB-B), 3.4 (AB-C) and 21.1 (AB-D) meters for the cutoff wavenumbers $k_x = 0.78$, 0.86, 0.92 and 1.19, respectively, observed in the growth-rate curves $\omega_i(k_x)$ in Fig. 10a. Qualitatively, the growth-rate curves show a cutoff at high wavenumber of the unstable spectrum, as in the work of Kuroki and Kishi (1984). Conversely, when k_x drops to zero, there is a positive asymptote, which we interpreted in the same way as Seminara (2010): "as bars develop in space, care must be taken in interpreting laboratory observations, which likely depend on the size of the experimental facility."

For case AB-B corresponding to Run 2 in Moteki et al. (2023), we illustrate the time evolution of sandbars on flat beds using the bed elevation contours at times $\hat{t} = 2, 10, 20$ and 60 min (see the four panels d-g in Fig. 10). At early times (i.e., $\hat{t} = 2 \text{ min}$), water was forced to flow over the planed bed, while oblique and fish-scale patterns called *rhomboid bars* were formed. The wavenumber of the observed disturbances fell within the range of the antidune instability (see the green dot and the green dashed line in Fig. 10a). Originally, for case AB-D, Ikeda (1983, Sections 3.4 and 5.1) reported a similar process when bars formed on flat beds of fine gravel, as shown in our Fig. 1d. Again, the measured wavenumber lies within the interval of antidune instability (marked by the red dot and the red dashed line in Fig. 10a). As flow continued in case AB-B, rhomboid bars immediately merged into larger rhomboid bars, and a train of antidunes appeared at the end of the flume at t=10 min with similar wavenumbers as those observed in the earliest stage of bar development. As time went on, the bedforms progressed as described originally by Ikeda (1983): "alternating bars are a more stable bed configuration, and with time, rhomboid bars gradually changed into alternating bars; the wavelength of alternating bars increased with longer flow duration." Alternate bars are indeed clearly visible at t = 60 min in case AB-B (Fig. 10g) and t = 73 min in case AB-D (Fig. 1c), with wavelength in agreement with the theoretical results (see the green/red square symbols and the solid lines in Fig. 10a). Interestingly, in case AB-C representing Run 3 of Inoue et al. (2020), the triple-row antidunes—already analyzed as cases AD-C in Section 3.2—persisted in the upstream part of the flume at later times. They are marked with the blue dot in the bed elevation contours at the top of Fig. 10 (panel b) and shown in the photograph on its right-hand side (panel c). The plane bed condition imposed at the flume inlet by the boundary condition probably allowed the antidune to be the dominant mode (antidunes are absolute instability migrating upstream). In contrast, in the downstream part of the flume, the alternate bar disturbed the uniform base flow, and became dominant (alternate bars are convective instability migrating downstream). The wavenumbers observed for both bedforms in the experiment exhibit the maximum growth rate in our theory, as indicated by the blue square over the blue solid line and the blue dot over the blue dashed line in Fig. 10a. On this occasion, we measured the antidune wavelength directly on the photograph at the end of the experiment, which gave a better agreement for the wavenumber than that reported previously in Section 3.2. In summary, these results further confirm that our approach can predict the development of both instabilities within a single theoretical framework.

Here, we have also considered two case studies of multiple bars, MB-A with $\beta = 116.7$ and MB-B with $\beta = 219$, corresponding to experiments B4 and C8 by Fujita (1989), respectively (see Table 4). Estimates of the multiple bar parameters were measured from the sketches of

bedform development in Fig. 7 and Fig. 10b by Fujita (1989), which are included in our Fig. 11. Following Ikeda's approach, Fujita (1989) monitored the transient state of bar formation and proved that multi-row bars and alternate bars exhibited similar features before reaching the equilibrium wavelength. In the first stage of the development, small-amplitude multi-row bars formed with a higher wavenumber than at later times when the bar was fully developed. In the second phase, the initially selected higher-order modes grouped together to form lower-order patterns. The bars therefore increased in length, moved downstream and combined, with generally a decrease in the number of rows. Finally, the bars formed in the previous phase increased in amplitude and wavelength to reach the characteristic final shape of the saturated nonlinear regime. Qualitatively, the development of multi-row bars resembled that of alternate single-row bars: it showed a similar increase in wavelength during growth (Fujita and Muramoto, 1985; Boraey, 2014; Seki et al., 2023), as explained above and shown in Fig. 10.

Table 4 reports the characteristic dimensions, the flow properties and the nondimensional parameters for the selected experiments taken from Fujita (1989). The two MB-A and MB-B cases have Froude numbers close to unity (0.79 $\leq \mathcal{F}t \leq 0.97$). For the roughness values in the experiments (i.e., $0.034 \leq d \leq 0.112$), the aspect ratio β , which varies from 115 to 219, is above the threshold required for the existence of multiple bars $\beta > 25 d^{-1/3}$ (Ahmari and Da Silva, 2011). For the dimensionless parameters, the main difference between the MB-A and MB-B cases is the value of β , which was substantially higher than in the AB-A to AB-D cases. The long duration of Fujita's experiments allowed for a detailed analysis of the bed evolution. The MB-A case finally led to the double-row mode, also known as the central bar mode, which corresponds to m=4. When bars started to form (stage I), the MB-A case was characterized by transverse modes with a higher m value than at later times (for stages II and III). In particular, we observe m=12 at $\widehat{t}=32$ min and m=8 at $\widehat{t}=1$ h and 38 min and $\widehat{t}=2$ h 33 min. In stage II, it was not easy to single out a specific mode precisely, for instance, at $\widehat{t}=2$ h and 33 min in MB-A or $\widehat{t}=30$ min in MB-B. We only give in Table 4 the most objective data, including the modes, wavelengths, and wavenumbers of the bars identified and measurable in Figures 11a-b at different times.

Figure 11c summarizes our theoretical results by plotting the growth-rate curves $\omega_i(k_x)$ for the MB-A and MB-B case studies. The amplification factor of the multiple bars is represented by a solid line, and, for completeness, we have also included the alternate bar as dashed line. The symbols on the solid-line curves indicate the wavenumbers identified experimentally. For nearly all the observed modes, the wavelength that was experimentally determined is quite close to the maximum growth rate. Surprisingly, the k_x estimates from the sketches in Fig. 11a-b are fairly consistent with the values predicted by our model. The unstable region for multi-row bars $(m \ge 4)$ appears for lower values of the wavenumber, as in the case of alternate bars (m = 1). Again, a horizontal asymptote exists on ω_i as k_x becomes vanishing small. When k_x increases, ω_i rises until reaching a maximum, and then ω_i decreases sharply, becoming negative (i.e., stable) at high wavenumbers. The growth-rate curves are shifted to the right for increasing m values, and the amplitude of the growth rate increases. Another interesting result is that no alternate bars were observed in any of the runs, probably because the growth rate ω_i decreases with decreasing mode m. Indeed, ω_i is much lower for m=1 than for $m\geq 4$. Another reason is the cutoff wavenumbers (i.e., $k_x = 1.33$ for MB-A and $k_x = 1$ for MB-B). The minimum wavelength required for an alternate bar to grow $(\omega_i > 0)$ is therefore $\Lambda_x = 14.2$ m in the MB-A case, and 11.3 m in the MB-B case. For MB-B, this condition is incompatible with the 15-m flume length, which is too short. These findings confirm that alternate bars (m=1) were unlikely to be observed in these experiments.

	\mathcal{F} r			β	d		k	
	Min	Max	Min	Max	Min	Max	Min	Max
Roll Wave (RW)	1.96	10.20	11.45	495.45	0.0008	0.004	0.037	0.08
Antidune (AD)	0.70	2.34	2.22	85.33	0.0014	0.575	0.292	1.74
Alternate Bar (AB)	0.27	2.01	3.53	54.35	0.0030	0.395	0.007	0.39
Multiple Bar (MB)	0.27	2.16	34.09	367.35	0.0060	0.617	-	-
Dune (DU)	0.20	0.76	0.90	20.33	0.0006	0.014	0.321	5.78
AB & AD	0.78	1.76	3.77	34.08	0.0146	0.177	0.017	1.17

Table 5: Minimum and maximum values of the control parameters and nondimensional wavelength in the experimental dataset.

3.4. Dimensionless characterization of bedform regime

In this section, we compare our theory with existing flume experiments on roll waves, antidunes and bars. To this end, we evaluated the three dimensionless parameters characterizing bedforms at equilibrium $\mathcal{F}\iota$ (14), ℓ (15) and ℓ (16), and plotted them in Fig. 12a. The data sources are listed for antidunes in Carling and Shvidchenko (2002) and Recking et al. (2009); for roll waves, the experiments were described by Brock (1969), Zhao et al. (2015) and in Section 3.1 for the Oroville spillway; the data sources on alternate bars are provided by Redolfi (2021) and Cheng and da Silva (2023); for multiple-row bars, we used Fujita (1989), among other references contained in Ahmari and Da Silva (2011); and, to complete the analysis, we included the data on dunes in channels provided by Cheng (2016) and Bradley and Venditti (2017), as well as our previous theoretical results, to study the factors that allow for the distinction of two-dimensional bedforms (Bohorquez et al., 2019). Two important observations can be made from Fig. 12a. First, the scatter plots of the roll waves (blue squares), multi-row bars (purple hexagons), and dunes (red diamonds) occupy parameter space regions that do not overlap with those of the other bedforms. Second, the antidunes (green points) and alternate bars (yellow triangles) overlap in a specific region, bounded by a gray area and a dashed line. The limits of the envelope of each bedform are given in Table 5.

As shown in Figure 12, we propose a simple three-dimensional representation that reveals a region of coexistence between antidunes and alternate bars. To determine this region, we first computed the single three-dimensional boundary that enclosed all points of each type of bedform. Then, we estimated the intersection of the volumes of antidunes and alternate bars using the algorithm of Möller (1997). The experiments used to determine the coexistence region come from different authors and distinct experimental setups. There is no single bedform type for a given set of parameters. For the same dimensionless parameters, some authors reported antidunes whereas others observed alternate bars. For instance, the antidune data showing the coexistence region come from Shaw and Kellerhals (1977), Cao (1985) (runs 127, 322, 323 and 324), Recking et al. (2009) (runs 1 and 2) and Inoue et al. (2020). This point confirms that the same experiment can lead to both instabilities concurrently, as shown in four runs of Inoue et al. (2020). Furthermore, dunes over alternate bars have been observed experimentally by da Silva (1991) and Valentine et al. (2001), which justifies the smaller subregion in the three-dimensional space $\{\mathcal{F}\tau, \mathcal{A}, \beta\}$ where dunes and alternate bars coexist (see Figure 12a).

Technical literature has generally used two-dimensional representations for the partitioning of bedforms, as is seen in the classic books on sediment transport; e.g., García (2007, Ch. 2), Julien (2010, Ch. 8), da Silva and Yalin (2017, Ch. 2) and Dey (2024, Chs. 8 and 9), among other authors. For instance, Figure 12b shows the projection of the three-dimensional scatter of Fig. 12a onto the two-dimensional parameter space $\{\beta, \mathcal{F}t\}$, which loses the θ -axis. Alternatively, Athaullah (1968)

and Vanoni (1974) maintained the dependency on the relative flow depth $\hat{\eta}_0/\hat{d} = \ell^{-1}$ and omitted the influence of the aspect ratio β in their analysis of two-dimensional bedforms. Figure 12c is the two-dimensional representation resulting from the dataset shown in Fig. 12a. This representation yields an unexpected result: the upper limit of the alternate bars (dashed line), along the relative submergence range $10 \le \ell^{-1} \le 200$ is close to the critical value $\mathcal{F}_{\ell} = 4.89 \ell^{0.33}$ (dashed-dotted line) established by Athaullah (1968), which marks the transition between the lower and upper regimes. It should be noted that Athaullah (1968) did not use alternate-bar data in his analysis. Instead, he employed Gilbert's (1914) dune experiments to delineate the transition from the lower to the upper regimes across the region $10 \le \ell^{-1} \le 10^2$ and $0.6 \le \mathcal{F}_{\ell} \le 1.7$, which is covered by antidunes and alternate bars in our Fig. 12c. For this reason, and in accordance with Southard and Boguchwal (1997), we believe that the classification proposed by Gilbert should be abandoned, even though it has become classical. Lastly, Fig. 12d shows the data in the $\{\beta, \ell^{-1}\}$ -plane. This classification dates back to Muramoto and Fujita (1977), and was then used by da Silva (1991) and co-workers (Ahmari and Da Silva, 2011; Cheng and da Silva, 2023) to determine the regions of existence for alternate bars, multiple bars and meanders.

The discriminant factors for bedforms in two-dimensional space $\{\beta, \mathcal{F}t\}$ (Fig. 12b), $\{d^{-1}, \mathcal{F}t\}$ (Fig. 12c), and $\{d^{-1}, \beta\}$ (Fig. 12d) show a misleading superposition between dunes and alternate bars, as well as between dunes, antidunes, and roll waves. We cite Athaullah (1968, pp. 51): "the common deficiency in such an approach is an inadequate demarcation of flow regimes by two independent parameters". In the three-dimensional space of Fig. 12a, an overlapping region is visible between alternate bars and antidunes. This region needs to be first defined in the three-dimensional space, as shown in Fig. 12a, and then projected onto the desired two-dimensional diagram. In doing so, we obtain the area bounded by a thick dashed line in panels b—d of Fig. 12. It should also be noted that there is a much smaller second region of coexistence for dunes and alternate bars, which has been omitted in our representations for clarity.

Figure 13a shows another discriminant factor of bedforms in the three-dimensional axes $\{d, k, \mathcal{F}\iota\}$. This representation was originally proposed in our earlier work (Bohorquez et al., 2019) to incorporate the additional parameter d into the $\{k, \mathcal{F}\iota\}$ -plane bedform chart originally created by Kennedy (1963). The diagram for $\{k, \mathcal{F}\iota\}$, shown in Fig. 13b, is one of the most commonly employed partitioning of bedforms used for verifying linear-stability theories published since the pioneering work of Kennedy (1969). Among other authors, Charru et al. (2013), Seminara (2010), and Dey and Ali (2020) used it. When projecting the $\{d, k, \mathcal{F}\iota\}$ space onto Kennedy's plane (see Fig. 13b), we observe that each bedform occupies a distinct region of the parameter space, with no overlap between the different bedforms. The three- or two-dimensional representation does not include multiple-row bars because of the absence of accurate measurements in the literature (Ahmari and Da Silva, 2011). Furthermore, using our wavelength estimates in Section 3.3, we confirm that in the three-dimensional space $\{d, k, \mathcal{F}\iota\}$, the multiple-row bars overlap with the point cloud of alternate bars.

Permanent roll waves exhibit a narrow range of the longitudinal wavenumber $k \approx 0.055 \pm 0.025$ for a wide range of Froude values $2 < \mathcal{F}\tau < 10$, and the dimensional wavelength $\widehat{\Lambda}_x$ scales with the dimensional flow depth $\widehat{\eta}_0$ as $\widehat{\Lambda}_x \approx 114\,\widehat{\eta}_0$ for roll waves. This functional dependency coincides with that of dunes produced by fully rough flows. Indeed, the average length of dunes given by Yalin (1977) was $\widehat{\Lambda}_x = 2\pi\,\widehat{\eta}_0 \approx 6\,\widehat{\eta}_0$, i.e., k = 1 (see also Zhou and Mendoza, 2005). Available correlations have been reviewed by Bradley and Venditti (2017). The constant of proportionality in the correlation equations differs substantially between roll waves and dunes. In Fig. 13c, we

extend Yalin's analysis and find out that the data on antidunes cover a broad range of relative submergence, and do not deviate too much from the predictions of the dune correlation equation. Although the scatter is large, the length of the alternate bars is close to the estimates given by the roll wave correlation equation. There is therefore a qualitative difference between the lengths of the roll-waves/alternate-bars and dunes/antidunes. This difference is explained by the dominant coarsening dynamics of roll waves (Chang et al., 2000), and the time-varying wavelength of alternate bars where the initially selected higher-order modes coalesce to form lower-order patterns (see Fujita and Muramoto, 1985). Such mechanisms can increase the wavelength by an order of magnitude.

We used the three-dimensional representation of the experimental data in Fig. 13a to test our linear-stability theory, similarly to what was done in the previous analyses of two-dimensional antidunes and roll waves (see Fig. 8). To this end, we defined the critical Froude number $\mathcal{F}_{cr}(k, \ell; \beta, m)$ as a function of the wavenumber k and roughness ℓ , with fixed values of β and m. This determination involved solving for $\omega = \omega_r$ in the eigenproblem $\mathbf{M} \cdot \mathbf{T} = 0$ (33)–(34) under the neutral stability condition $\omega_i = 0$, which corresponds to a zero growth rate. The present theory identifies three potential instabilities: the roll wave (Section 3.1), the antidune (Section 3.2), and the bar (Section 3.3). These instabilities delineate three regions in the parameter space $(\mathcal{F}_{\ell}, d, k)$, which are defined by $\Im \tau > \Im \tau_{cr}^{RW}$, $\Im \tau > \Im \tau_{cr}^{AD}$ and $\Im \tau < \Im \tau_{cr}^{AB}$, respectively, for any β and m. In order to maintain consistency with the experimental observations, we systematically varied the aspect ratio from $\beta = 1$ to 500, and the transverse mode from m = 0 (two-dimensional instability) to m = 18 (multi-row instability), thereby establishing the boundaries of the unstable regions (see Fig. 13d). The surface shaded in grey \mathcal{F}_{cr}^{PB} represents the plane bed condition $Sh_{cr} = 0.02$, which was the threshold for sediment motion. In this plot, we have also drawn the neutral curve that defines the region $\Im z < \Im z_{cr}^{DU}$ for the growth of two-dimensional dunes (i.e., m=0) as we did in our previous work (Bohorquez et al., 2019).

4. Conclusions

In this article, we studied flow-transverse bedforms and roll waves, focusing specifically on their conditions of existence and dynamics. The linear stability properties of the morphodynamic model (1)–(4) determine the type of instability depending on three dimensionless numbers (i.e., the Froude number \mathcal{F}_{ℓ} , the grain roughness relative to the water depth ℓ , and the width-to-depth ratio β), the lateral mode m, and the scaled streamwise wavenumber k. To validate our results, we have considered more than 800 experimental runs from the literature and selected representative case studies of multi-train antidunes, three-dimensional antidunes, alternate bars, and multiple bars, all of which were overlooked in previous stability theories. For multi-row roll waves, we preferred real-world data to laboratory data because more extensive information was found on the service spillway of the Oroville Dam. Overall, our theory is in agreement with the experiments, enabling us to draw the following conclusions.

A crucial part of our work has been to identify and delineate the regions across the parameter spaces $\{\mathcal{F}\iota, \mathcal{d}, \beta\}$ (Fig. 12) and $\{\mathcal{F}\iota, \mathcal{d}, k\}$ (Fig. 13) where antidunes, bars, and roll waves can occur. For the sake of completeness, we have also included our earlier results on dunes. The three-dimensional diagrams establish a classification scheme of free-surface instability (i.e., roll wave) and bedforms (i.e., dunes, antidunes, and bars) based on quantitative objective criteria. Through these diagrams, it becomes possible to intertwine fluid dynamics, sediment size, channel shape, and the morphology of bedforms and roll waves by means of the dimensionless parameters $\mathcal{F}\iota$, \mathcal{d} , β , and k. The surprising complexity in flows over fixed and erodible beds includes multiple regimes

when the dimensionless parameters \mathcal{F}_{ℓ} , \mathcal{J} , and β are comparable. The most striking example is that of antidunes and bars coexisting in the same channel experiments. The second example is provided by the apparent disagreement between experimenters who reported alternate bars and those who observed antidunes or dunes for the same dimensional numbers. In both examples, the morphology of each bedform differs (i.e., bars are larger than dunes and antidunes), and interestingly, no points overlap in the trivariate plot of \mathcal{F}_{ℓ} , \mathcal{J} and k in Fig. 13. This disagreement provides clear evidence that bedform type and geometry are not fixed in one way only. The third example involves channels with a high width-to-depth ratio that are subject to the same flow conditions. In some cases, the roll wave maintains its shape across the channel width, as it does in narrow channels, whereas in other cases, multiple rows develop. Rhomboid, multiple and alternate bars—as well as multi-row antidunes and three-dimensional antidunes—may also develop over time in the same experimental run. These phenomena suggest that environmental flows can result in different sedimentary records, even when streamflow, sediment transport rate, and channel geometry are the same. Hence, bedform superposition can develop in straight alluvial rivers and channel streams under steady uniform flow.

We presented a simple morphodynamic model based on the Saint-Venant–Exner equations (1)–(2), (4) and non-capacity bedload equation (3), and the model's linear stability analysis shows that all the aforementioned types of instability can develop over time. To maintain consistency with classic works on bedform discriminators, we concentrated on the type of bedform. Due to the limitations of a three-dimensional representation in a physical problem with five variables, we disregarded the influence of the remaining parameters m and β . When m and β are varied within the same range of values as in the entire data set, our theory predicts the regions of the parameter space $\{\mathcal{F}\tau, \mathcal{A}, k\}$, in which each type of instability can grow. When considering additional factors controlling the convective and absolute nature of instability and calculating the intersections of the unstable limits $\mathcal{F}\tau_{cr}^{RW}$, $\mathcal{F}\tau_{cr}^{AD}$, $\mathcal{F}\tau_{cr}^{AB}$ and $\mathcal{F}\tau_{cr}^{DU}$ shown in Fig. 13d, we can delineate the specific subdomains of Fig. 14 for antidunes (green), bars (yellow), roll waves (blue), and dunes (red). The resulting diagram is in agreement with more than 800 flume experiments, which fall within the expected instability regions. Some important aspects are the following:

- 1. The Froude numbers of the antidune experiments have the lower limit \mathcal{F}_{cr}^{AD} . The experimental wavenumbers are restricted to a narrow range of the unstable spectrum owing to the absolute nature of the hydrodynamic instability. This means that, for a specific experiment with known parameters \mathcal{F}_{ℓ} , \mathcal{J} , and β , the wavenumber k is the most unstable and could be predicted theoretically.
- 2. For alternate bars, the Froude numbers of most experiments are consistent with the upper limit \mathcal{F}_{cr}^{AB} . The experimental wavenumbers occupy a substantial portion of the unstable domain. There are two reasons for this: (i) the system is convectively unstable, thereby amplifying any disturbances present in the experimental setup within the unstable wavelength or frequency range; (ii) the dynamics of coarsening and coalescence of the alternate bars influence the wavelength measured experimentally in the nonlinear regime.
- 3. Another bedform associated with convective instability is the dune. Dunes develop at lower Froude numbers than alternate bars, specifically $\mathcal{F}\iota < 0.76$, and higher wavenumbers, $k \geq 0.32$, which is consistent with the critical surface of alternate bars.
- 4. For roll waves, the experiments provide another evidence for the theoretical condition $\mathcal{F}_{t} > \mathcal{F}_{cr}^{RW}$. Furthermore, this region of space is exclusively occupied by free-surface hydrodynamic instability. No bedform has been observed experimentally due to the tendency of the flow to

erode any bedform at such high Froude (or Shields) values.

We conclude that depth-averaged equations such as the Saint-Venant equations are able to describe and predict a number of characteristics of flows on an erodible and/or steep bed despite their relative simplicity. Two important ingredients are (i) the existence of a diffusive term in the source term (Boussinesq-type turbulent viscosity) of the momentum balance equation, and (ii) a non-unique relationship between particle activity and bottom stress.

Projecting three-dimensional representations onto two-dimensional diagrams facilitates comparison with traditional bedform discriminators or charts, such as those by Kennedy, Vanoni, da Silva, and Yalin. Alternative representations that replace \mathcal{F}_{ℓ} by the Shields number Sh or the bed slope S can also be easily plotted. The dataset and Matlab scripts with the linear stability codes used to plot the figures are openly available. These types of representations have numerous applications in hydraulic engineering, paleohydrology, and fluvial geomorphology.

Declaration of competing interest

The authors declare that they have no known competing financial interests or personal relationships that could have appeared to influence the work reported in this paper.

Data availability

The codes for the linear-stability analysis and the processed dataset supporting the findings of this study are openly available at https://doi.org/10.5281/zenodo.17313974. We defer the sharing date to ensure they are released simultaneously with the associated article. All experimental data are available in the cited literature and the Tables 1-4.

Acknowledgments

Funding for open access charge: Universidad de Jaén/CBUA. Patricio Bohorquez acknowledges the support of the European UnionNextGenerationEU/PRTR and MCIN/AEI (grant No. TED2021-129910B-I00). Christophe Ancey acknowledges the support of the Swiss National Science Foundation (grant No. 200020_204108). Daniel Vito Papa acknowledges the support of Agence de l'Innovation de Défense (AID) and Centre Interdisciplinaire d'Études pour la Défense et la Sécurité (CIEDS) (grant No. 2021-ICING). We are thankful to the reviewers for their time and insightful suggestions. Their work has helped to identify weaknesses in the first version, which has allowed us to improve the presentation of the approach and the results. Among the reviewers, we thank Arnoud Slootman, who accepted to reveal his identity.

Appendix A. Nomenclature

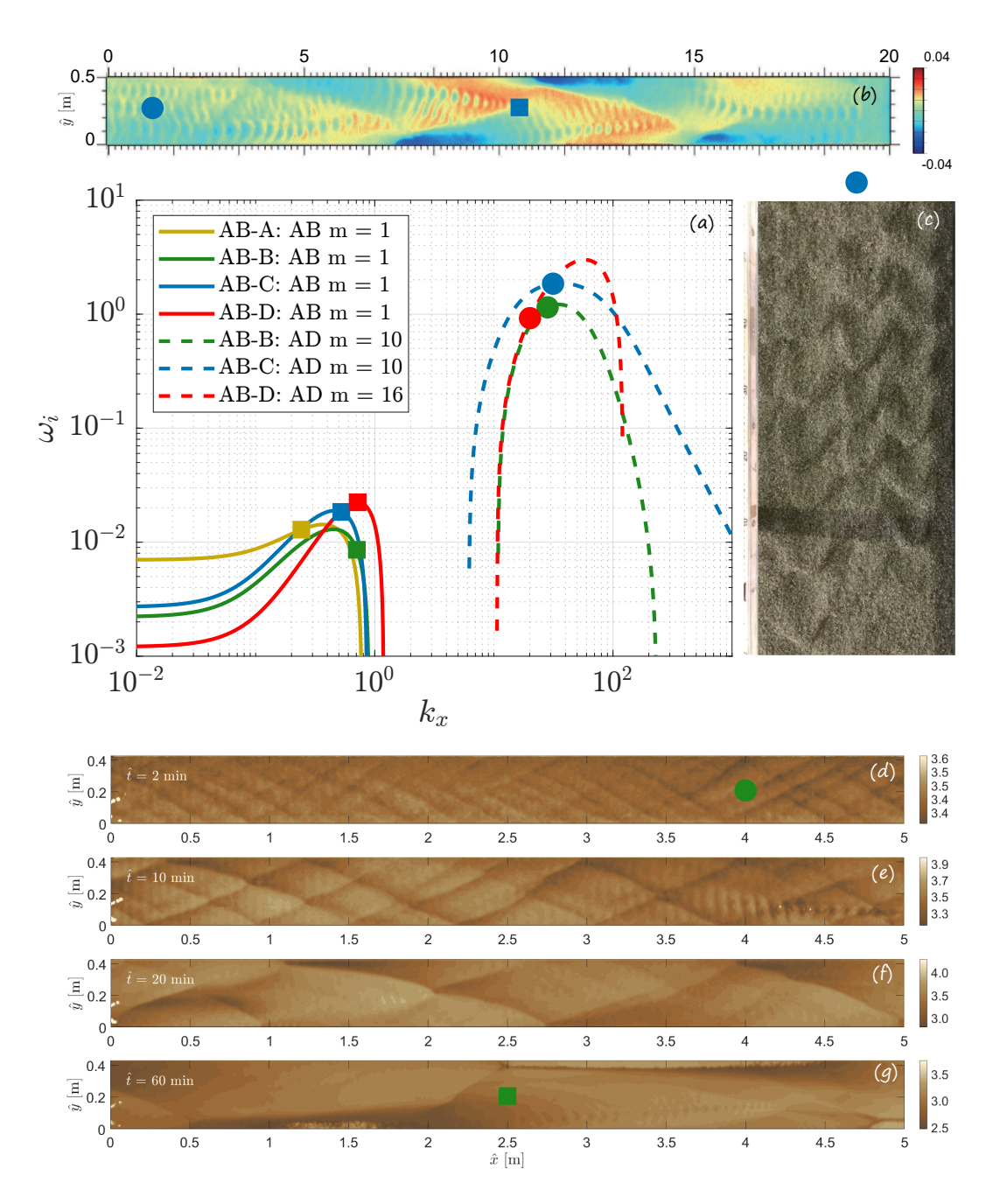


Fig. 10: (a) Continuous lines show the curves of the growth rates $\omega_i(k_x)$ of the bar eigenvalue for the mode m=1 related to the formation of alternate bars at late times in Run-63 by Jaeggi (1984) (case AB-A), Run 2 by Moteki et al. (2023) (case AB-B), Run 3 of Inoue et al. (2020) (case AB-C) and Run 80 of Ikeda (1983) (case AB-D). Dashed lines are the growth rate curves for the antidune eigenvalue for the higher-order mode observed in cases AB-B, AB-C and AB-D. The bed elevation contour and the antidunes plan view in panels b-c are reproduced from Fig. 10 in Inoue et al. (2020) and were taken at the end of the experiment when the water flow ceased. The bed levels in panels d-g show the transient stages during the development of alternate bars in Run 2 Member 1 of Moteki et al. (2023) at the times $\hat{t}=1$, 10, 20 and 60 minutes (data processed from scratch from Moteki et al., 2022). For case AB-D, see the photographs by Ikeda (1983) of rhomboid bars and alternate bars already shown in Fig. 1c and 1d, respectively. The symbols in panel (a) indicate the experimental wavenumbers given in Table 4.

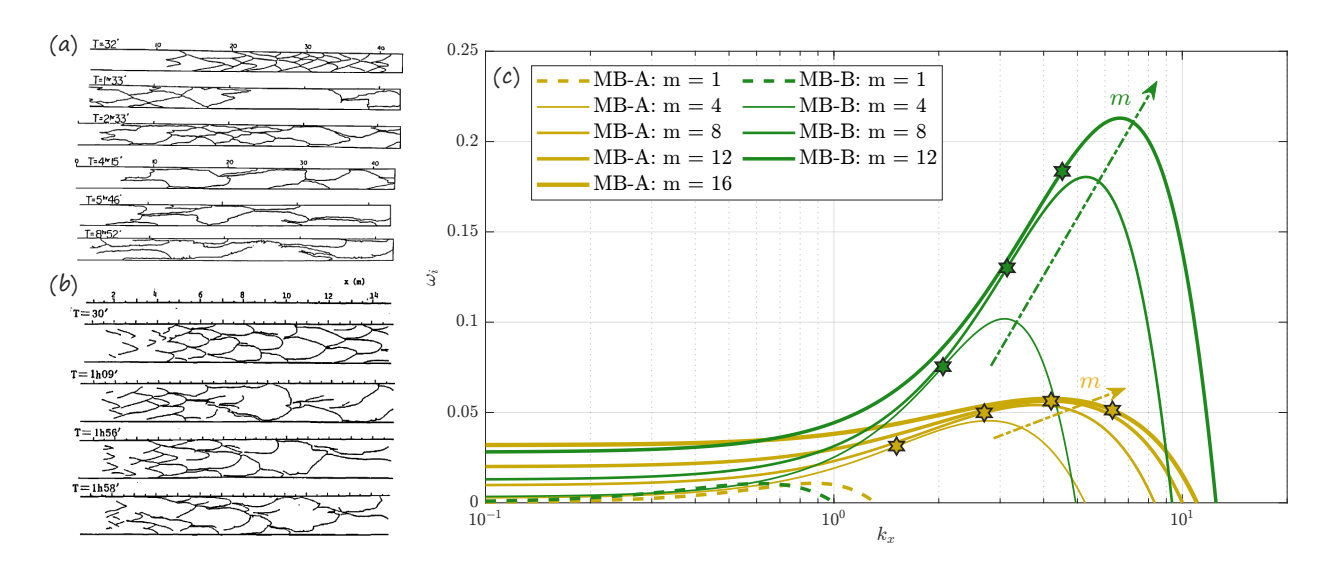


Fig. 11: Sketches of the bed evolution for Runs (a) B4 and (b) C8 by Fujita (1989, Fig. 7 and 10b), referred to as cases MB-A and MB-B, respectively, in the panel (c) showing the theoretical growth rate of the bar eigenvalue for the transverse modes observed in the experiments. The symbols correspond to the wavenumbers given in Table 4.

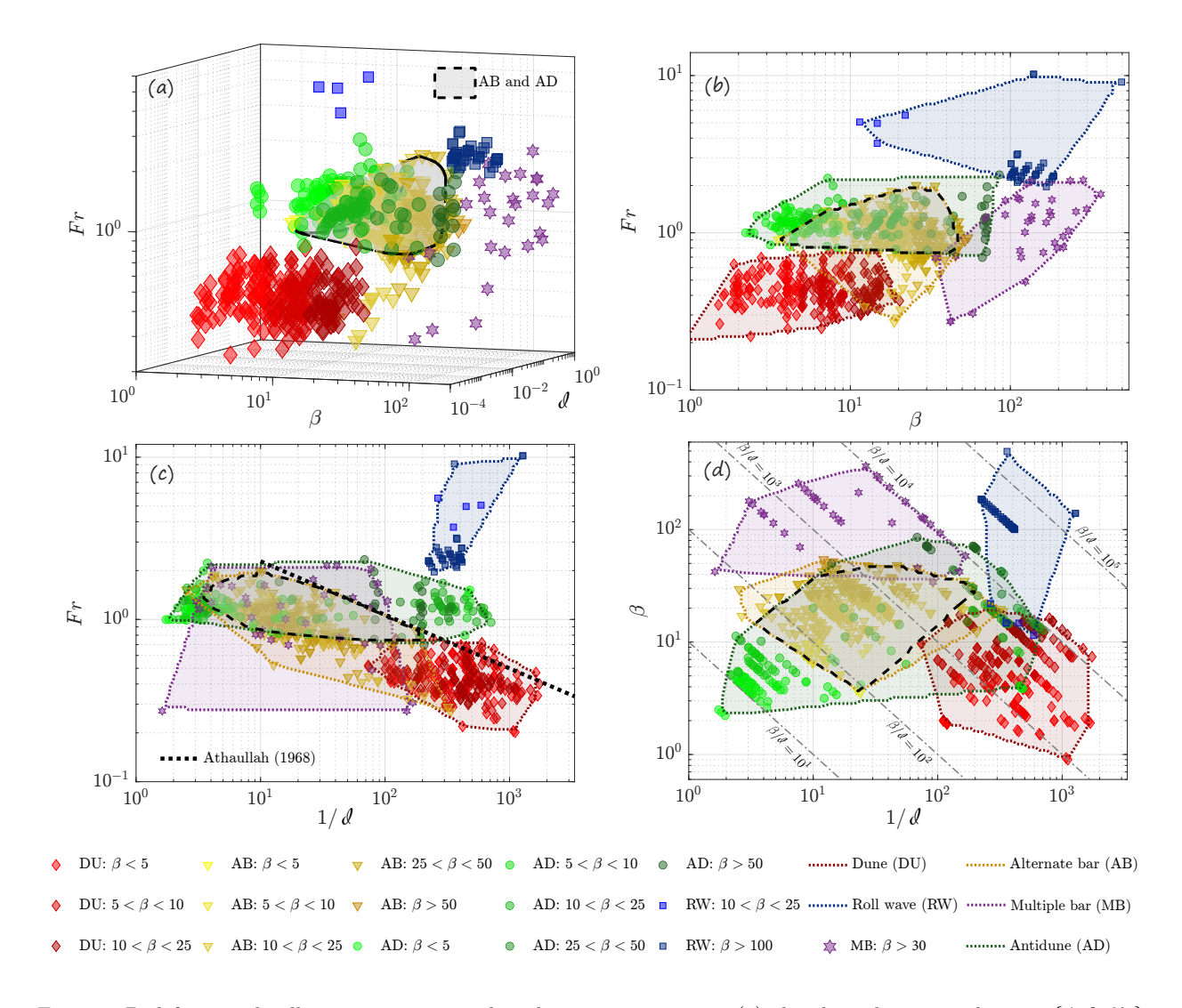


Fig. 12: Bed form and roll wave partitioning based on experiments in (a) the three-dimensional space $\{d, \beta, \mathcal{F}\iota\}$ developed in this work, and the two-dimensional projections in the planes (b) $\{\beta, \mathcal{F}\iota\}$, (c) $\{d^{-1}, \mathcal{F}\iota\}$ originally used by Vanoni (1974) for two-dimensional bedforms and (d) $\{d^{-1}, \beta\}$ proposed by da Silva and Yalin (2017) specifically for alternate bars.

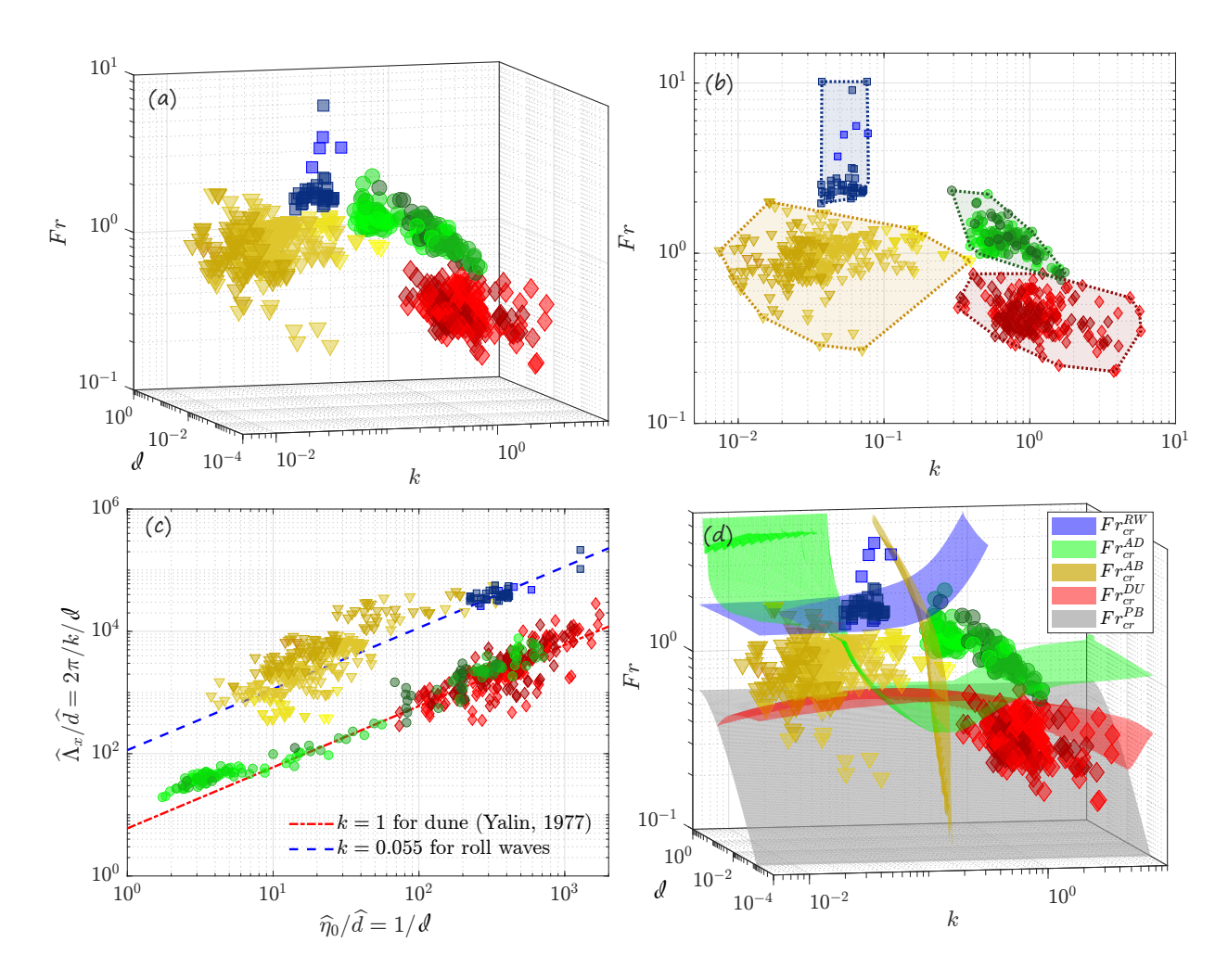


Fig. 13: (a) Bed form and roll wave discriminators based on experiments in the three-dimensional space $\{\ell, k, \mathcal{F}\iota\}$ used originally in Bohorquez et al. (2019). (b) Projection in the two-dimensional space $\{k, \mathcal{F}\iota\}$ of Kennedy (1963). (c) Yalin (1977) diagram of the nondimensional longitudinal wavelegth $\widehat{\Lambda}_x/\widehat{d}$ as a function of the relative submergence ℓ^{-1} . (d) Regions of the space $\{\ell, \mathcal{F}\iota\}$ compatible with the development of roll waves (in blue), antidunes (in green), alternate bars (in yellow) and dunes (in red) predicted by our linear-stability theory in agreement with flume experiments.

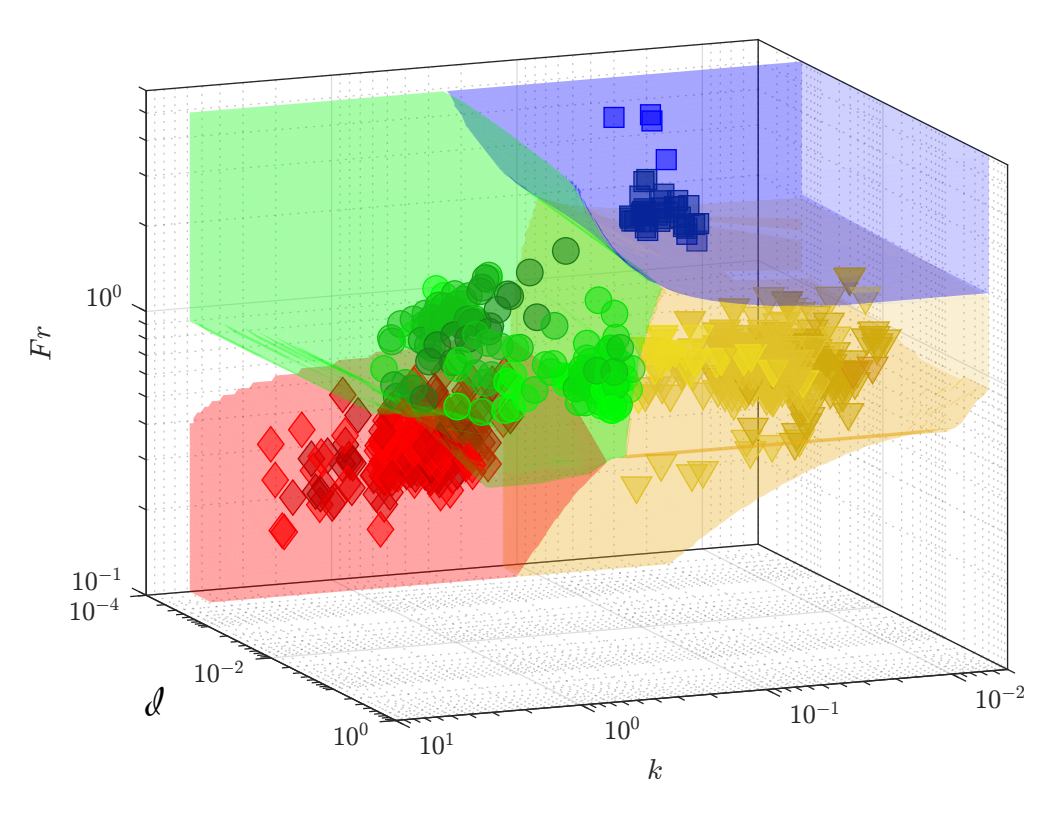


Fig. 14: Existence regions of antidunes (green), rollwaves (blue), bars (yellow), and dunes (red) in the proposed theory (enclosed volumes) regarding flume experiments (symbols).

Table A.6: Roman symbols

Symbol	Units	Description
\overline{a}	_	sediment-to-water velocity ratio
\widehat{B}	m	channel width
c_t	_	turbulent constant parameter
$\frac{c_t}{\widehat{d}}$	m	mean diameter of the grains
d	_	grain roughness relative to the water depth
f	_	Darcy-Weisbach friction factor
$\mathcal{F}r$	_	Froude number
\widehat{g} i	$\mathrm{m/s^2}$	gravitational acceleration
i	_	imaginary number
I	_	identity tensor
k	_	streamwise wavenumber based on water depth
\widehat{k}_s	m	bed roughness size
k_x	_	streamwise wavenumber based on channel width
k_y	_	cross-stream wavenumber based on channel width
m	_	lateral Fourier mode
\widehat{Q}	m^3/s	water discharge
s	_	particle-to-water density ratio
S	_	bed slope
Sc	_	turbulent Schmidt number
Sh	_	Shields number
Sh_{cr}	_	Shields threshold of incipient motion
\widehat{t}	\mathbf{s}	time
\widehat{u}	m/s	streamwise velocity component
$\widehat{m{u}}$	$\mathrm{m/s}$	depth-averaged velocity vector
$\widehat{m{u}}_p$	$\mathrm{m/s}$	mean velocity vector of moving particles
$\widehat{m{u}}_*$	$\mathrm{m/s}$	friction velocity
\widehat{v}	$\mathrm{m/s}$	cross-stream velocity component
\widehat{x}	\mathbf{m}	streamwise coordinate
\widehat{y} \widehat{z}	\mathbf{m}	cross-stream coordinate
\widehat{z}	m	bed elevation

References

- Ahmari, H., Da Silva, A.M.F., 2011. Regions of bars, meandering and braiding in da Silva and Yalin's plan. J. Hydraul. Res. 49, 718–727. doi:10.1080/00221686.2011.614518.
- Ancey, C., Bohorquez, P., Heyman, J., 2015. Stochastic interpretation of the advection-diffusion equation and its relevance to bed load transport. J. Geophys. Res. Earth Surf. 120, 2529–2551. doi:10.1002/2014JF003421.
- Ancey, C., Heyman, J., 2014. A microstructural approach to bed load transport: mean behaviour and fluctuations of particle transport rates. J. Fluid Mech. 744, 129–168. doi:10.1017/jfm. 2014.74.
- Ancey, C., Recking, A., 2023. Scaling behavior of bedload transport: what if Bagnold was right? Earth-Sci. Rev. 246, 104571. doi:10.1016/j.earscirev.2023.104571.

Table A.7: Greek symbols.

Symbol	Units	Description
$\widehat{\alpha}$	m^2/s	particle diffusivity tensor
β	_	width-to-depth ratio
$\widehat{\gamma}$	\mathbf{m}	particle activity (volume of moving particles per unit bed
		area)
$\widehat{\gamma}_{ss}$	\mathbf{m}	steady-state particle activity
$egin{array}{l} \zeta_b \ \widehat{\eta} \ \widehat{\kappa} \end{array}$	_	bed porosity
$\widehat{\eta}$	\mathbf{m}	water depth
$\widehat{\kappa}$	s^{-1}	deposition minus collective entrainment coefficient
κ_{γ}	_	dimensionless relaxation rate based on particle activity
κ_η	_	dimensionless relaxation rate based on flow depth
$egin{array}{l} \widehat{\Lambda}_x \ \widehat{\Lambda}_y \ \widehat{oldsymbol{ u}} \end{array}$	m	streamwise wavelength
$\widehat{\Lambda}_y$	\mathbf{m}	cross-stream wavelength
$\widehat{oldsymbol{ u}}$	$\rm m^2/s$	eddy viscosity tensor
$\widehat{\widehat{oldsymbol{ au}}}_b$	${ m kg/m^3}$	water density
$\widehat{m{ au}}_b$	Pa	bottom shear stress
ω	_	complex frequency
ω_i	_	growth rate (imaginary part of the complex frequency)
ω_r	_	real part of the complex frequency

- Anderson, L.G., 1953. The characteristics of sediment waves formed by flow in open channels, in: Proc. Third Mid-Western Conf. on Fluid Mech., University of Minnesota. pp. 379–395.
- Andreotti, B., Claudin, P., Devauchelle, O., Durán, O., Fourrière, A., 2012. Bedforms in a turbulent stream: ripples, chevrons and antidunes. J. Fluid Mech. 690, 94–128. doi:10.1017/jfm.2011. 386.
- Ashmore, P., 2013. 9.17 Morphology and Dynamics of Braided Rivers, in: Shroder, J.F. (Ed.), Treatise on Geomorphology. Academic Press, San Diego, pp. 289–312. doi:10.1016/B978-0-12-374739-6.00242-6.
- Athaullah, M., 1968. Prediction of bedforms in erodible channels. Ph.D. thesis. Colorado State University, Fort Collins, Colorado.
- Balmforth, N.J., Provenzale, A., 2001. Patterns of dirt, in: Balmforth, N.J., Provenzale, A. (Eds.), Geomorphological Fluid Mechanics. Springer, pp. 369–393. doi:10.1007/3-540-45670-8_15.
- Balmforth, N.J., Vakil, A., 2012. Cyclic steps and roll waves in shallow water flow over an erodible bed. J. Fluid Mech. 695, 35–62. doi:10.1017/jfm.2011.555.
- Barenblatt, G.I., 1996. Scaling, Self-similarity, and Intermediate Asymptotics: Dimensional Analysis and Intermediate Asymptotics. Cambridge Texts in Applied Mathematics, Cambridge University Press. doi:10.1017/CB09781107050242.
- Blondeaux, P., Seminara, G., 1985. A unified barbend theory of river meanders. J. Fluid Mech. 157, 449–470. doi:10.1017/S0022112085002440.
- Bohorquez, P., 2010. Competition between kinematic and dynamic waves in floods on steep slopes. J. Fluid Mech. 645, 375–409. doi:10.1017/S002211200999276X.

- Bohorquez, P., Ancey, C., 2015. Stochastic-deterministic modeling of bed load transport in shallow water flow over erodible slope: linear stability analysis and numerical simulation. Adv. Water Resour. 83, 36–54. doi:10.1016/j.advwatres.2015.05.016.
- Bohorquez, P., Ancey, C., 2016. Particle diffusion in non-equilibrium bedload transport simulations. Appl. Math. Model. 40, 7474–7492. doi:10.1016/j.apm.2016.03.044.
- Bohorquez, P., Cañada Pereira, P., Jimenez-Ruiz, P.J., del Moral-Erencia, J.D., 2019. The fascination of a shallow-water model for the formation of megaflood-scale dunes and antidunes. Earth-Sci. Rev. 193, 91–108. doi:10.1016/j.earscirev.2019.03.021.
- Boraey, A.A., 2014. Alternate bars under steady state flows: time of development and geometric characteristics. Ph.D. thesis. M.Sc. Thesis, Department of Civil Engineering, Queens University, Kingston.
- Bose, S.K., Dey, S., 2009. Reynolds averaged theory of turbulent shear flows over undulating beds and formation of sand waves. Phys. Rev. E 80, 036304. doi:10.1103/PhysRevE.80.036304.
- Bradley, R.W., Venditti, J.G., 2017. Reevaluating dune scaling relations. Earth-Sci. Rev. 165, 356-376. doi:10.1016/j.earscirev.2016.11.004.
- Brock, R.R., 1968. Development of Roll Waves in Open Channels. Ph.D. thesis. Rep. KH-R-16, 226 pp., W. M. Keck Lab. of Hydrol. and Water Resour. Calif. Inst. of Technol., Pasadena. doi:10.7907/E2V8-1794.
- Brock, R.R., 1969. Development of roll-wave trains in open channels. J. Hydraul Div. 95, 1401–1427. doi:10.1061/JYCEAJ.0002132.
- Brock, R.R., 1970. Periodic permanent roll waves. J. Hydraul Div. 96, 2565–2580. doi:10.1061/ JYCEAJ.0002801.
- California Department of Water Resources: California Data Exchange Center, . Stations ORO and Sensor Number 85. URL: https://cdec.water.ca.gov/. Accessed on 1st january 2025.
- California Deparment of Water Resources: Galleries, 2025. STATE WATER PROJECT/Dams/Oroville Dam. URL: https://pixel-ca-dwr.photoshelter.com/. Accessed on 1st january 2025.
- Callander, R.A., 1969. Instability and river channels. J. Fluid Mech. 36, 465–480. doi:10.1017/S0022112069001765.
- Camporeale, C., Ridolfi, L., 2011. Modal versus nonmodal linear stability analysis of river dunes. Phys. Fluids 23, 104102. doi:10.1063/1.3644673.
- Cao, H.H., 1985. Resistance hydraulique d'un lit à gravier mobile à pente raide; étude expérimentale. Ph.D. thesis. EPFL, Switzerland. doi:10.5075/epfl-thesis-589.
- Cao, Z., Hu, P., Hu, K., Pender, G., Liu, Q., 2015. Modelling roll waves with shallow water equations and turbulent closure. J. Hydraul. Res. 53, 161–177. doi:10.1080/00221686.2014. 950350.

- Carling, P.A., 2013. Freshwater megaflood sedimentation: What can we learn about generic processes? Earth-Sci. Rev. 125, 87–113. doi:10.1016/j.earscirev.2013.06.002.
- Carling, P.A., Shvidchenko, A.B., 2002. A consideration of the dune:antidune transition in fine gravel. Sedimentology 49, 1269–1282. doi:10.1046/j.1365-3091.2002.00496.x.
- Cartigny, M.J.B., Ventra, D., Postma, G., van Den Berg, J.H., 2014. Morphodynamics and sedimentary structures of bedforms under supercritical-flow conditions: New insights from flume experiments. Sedimentology 61, 712–748. doi:10.1111/sed.12076.
- Cea, L., Puertas, J., Vásquez-Cendón, M.E., 2007. Depth averaged modelling of turbulent shallow water flow with wet-dry fronts. Arch. Comput. Methods Eng. 14, 303–341. doi:10.1007/s11831-007-9009-3.
- Chan, H.C., Lin, Y.Z., Lin, P.W., 2025. The effect of channel slope on steep channel flow instability. Flow Meas. Instrum. 104, 102900. doi:10.1016/j.flowmeasinst.2025.102900.
- Chang, H.C., Demekhin, E.A., Kalaidin, E., 2000. Coherent structures, self-similarity, and universal roll wave coarsening dynamics. Phys. Fluids 12, 2268–2278. doi:10.1063/1.1287659.
- Charru, F., 2006. Selection of the ripple length on a granular bed sheared by a liquid flow. Phys. Fluids 18. doi:10.1063/1.2397005.
- Charru, F., Andreotti, B., Claudin, P., 2013. Sand ripples and dunes. Annu. Rev. Fluid Mech. 45, 469–493. doi:10.1146/annurev-fluid-011212-140806.
- Cheng, N., 2016. Comparison of sediment-pickup rates over plane bed and dunes. J. Hydraul. Eng. 142, 04016057. doi:10.1061/(ASCE)HY.1943-7900.0001204.
- Cheng, Y., da Silva, A.M.F., 2023. Empirical determination of free alternate bar length. J. Hydraul. Eng. 149, 04023027. doi:10.1061/JHEND8.HYENG-13245.
- Colombini, M., Seminara, G., Tubino, M., 1987. Finite-amplitude alternate bars. J. Fluid Mech. 181, 213–232. doi:10.1017/S0022112087002064.
- Colombini, M., Stocchino, A., 2012. Three-dimensional river bed forms. J. Fluid Mech. 695, 63–80. doi:10.1017/jfm.2011.556.
- Cornish, V., 1907. Progressive waves in rivers. The Geographical Journal 29, 23–31. doi:10.2307/1776113.
- Deigaard, R., 2006. Breaking antidunes: Cyclic behavior due to hysteresis. J. Hydraul. Eng. 132, 620–623. doi:10.1061/(ASCE)0733-9429(2006)132:6(620).
- Dey, S., 2024. Fluvial Hydrodynamics: Hydrodynamic and Sediment Transport Phenomena. 2nd ed., Springer Nature. doi:10.1007/978-3-031-26038-4.
- Dey, S., Ali, S.Z., 2020. Fluvial instabilities. Phys. Fluids 32, 061301. doi:10.1063/5.0010038.
- Di Cristo, C., Iervolino, M., Vacca, A., 2006. Linear stability analysis of a 1-D model with dynamical description of bed-load transport. J. Hydraul. Res. 44, 480–487. doi:10.1080/00221686.2006. 9521699.

- Di Cristo, C., Iervolino, M., Vacca, A., Zanuttigh, B., 2008. Minimum channel length for roll-wave generation. J. Hydraul. Res. 46, 73–79. doi:10.1080/00221686.2008.9521844.
- Di Cristo, C., Vacca, A., 2005. On the convective nature of roll waves instability. J. Appl. Math. 2005, 914047. doi:10.1155/JAM.2005.259.
- Dressler, R.F., 1949. Mathematical solution of the problem of roll-waves in inclined open channels. Comm. Pure Appl. Math. 2, 149–194. doi:10.1002/cpa.3160020203.
- Duró, G., Crosato, A., Tassi, P., 2016. Numerical study on river bar response to spatial variations of channel width. Adv. Water Resour. 93, 21–38. doi:10.1016/j.advwatres.2015.10.003.
- Federici, B., Seminara, G., 2003. On the convective nature of bar instability. J. Fluid Mech. 487, 125–145. doi:10.1017/S0022112003004737.
- France, J.W., Alvi, I.A., Dickson, P.A., Falvey, H.T., Rigbey, S.J., Trojanowski, J., 2018. Independent forensic team report: Oroville Dam spillway incident. Independent Forensic Team: Leiden, The Netherlands. URL: https://damsafety.org/sites/default/files/files/Independent% 20Forensic%20Team%20Report%20Final%2001-05-18.pdf.
- Fredsøe, J., 1978. Meandering and braiding of rivers. J. Fluid Mech. 84, 609–624. doi:10.1017/S0022112078000373.
- Fujita, Y., 1989. Bar and Channel Formation in Braided Streams. American Geophysical Union (AGU). chapter 13. pp. 417–462. doi:10.1029/WM012p0417.
- Fujita, Y., Muramoto, Y., 1982. Experimental study on stream channel processes in alluvial rivers. Bulletin of the Disaster Prevention Research Institute 32. URL: http://hdl.handle.net/2433/124906.
- Fujita, Y., Muramoto, Y., 1985. Studies on the process of development of alternate bars. Bull. Disas. Prev. Res. Inst., Kyoto University 35, 55–86.
- Fujita, Y., Muramoto, Y., 1988. Multiple bars and stream braiding, in: White, W. R. (Ed.), International Conference on River Regime, Hydraulics Research Limited, Wallingford, Oxon UK, Cambridge. pp. 289–300. doi:10.1017/CB09780511635632.002.
- Furbish, D.J., Fathel, S.L., Schmeeckle, M.W., Jerolmack, D.J., Schumer, R., 2017. The elements and richness of particle diffusion during sediment transport at small timescales. Earth Surf. Process. Landf. 42, 214–237. doi:10.1002/esp.4084.
- Furbish, D.J., Haff, P.K., Roseberry, J.C., Schmeeckle, M.W., 2012. A probabilistic description of the bed load sediment flux: 1. Theory. J. Geophys. Res. Earth Surf. 117, F03031. doi:10.1029/ 2012JF002352.
- García, M. (Ed.), 2007. Sedimentation Engineering. volume 110. ASCE Manuals and Reports on Engineering Practice, Reston.
- Garcia, M., Niño, Y., 1993. Dynamics of sediment bars in straight and meandering channels: Experiments on the resonance phenomenom. J. Hydraul. Res. 31, 739–762. doi:10.1080/00221689309498815.

- Garcia Lugo, G.A., Bertoldi, W., Henshaw, A.J., Gurnell, A.M., 2015. The effect of lateral confinement on gravel bed river morphology. Water Resour. Res. 51, 7145–7158. doi:10.1002/2015WR017081.
- Gilbert, G.K., 1914. The transportation of débris by running water. U. S. Geol. Surv. Prof. Pap. 86, 263 pp. doi:10.3133/pp86.
- Núñez González, F., Martín-Vide, J.P., 2011. Analysis of antidune migration direction. J. Geophys. Res. Earth Surf. 116. doi:10.1029/2010JF001761.
- Gradowczyk, M.H., 1968. Wave propagation and boundary instability in erodible-bed channels. J. Fluid Mech. 33, 93–112. doi:10.1017/S0022112068002387.
- Greco, M., Iervolino, M., Vacca, A., 2017. Analysis of bedform instability with 1-D two-phase morphodynamical models. Adv. Water Resour. doi:10.1016/j.advwatres.2017.07.002.
- Guan, M., Liang, Q., 2017. A two-dimensional hydro-morphological model for river hydraulics and morphology with vegetation. Environ. Model. Softw. 88, 10–21. doi:10.1016/j.envsoft.2016.11.008.
- Guo, J.C.Y., 1999. Roll waves in high gradient channels. Water Int. 24, 65–69. doi:10.1080/02508069908692136.
- Guy, H.P., Simons, D.B., Richardson, E.V., 1966. Summary of alluvial channel data from flume experiments, 1956-61. Water-Supply Paper 462-I, U.S. Geol. Survey, doi:10.3133/pp462I.
- Huang, D., Iwasaki, T., Yamada, T., Hiramatsu, Y., Yamaguchi, S., Shimizu, Y., 2023. Morphodynamic equilibrium of alternate bar dynamics under repeated hydrographs. Adv. Water Resour. 175, 104427. doi:10.1016/j.advwatres.2023.104427.
- Hwang, S.H., Chang, H.C., 1987. Turbulent and inertial roll waves in inclined film flow. Phys. Fluids 30, 1259–1268. doi:10.1063/1.866292.
- Ikeda, H., 1973. A study on the formation of sand bars in a experimental flume. Geographical Review of Japan 46, 435–451. doi:10.4157/grj.46.435.
- Ikeda, H., 1975. On the bed configuration in alluvial channels: Their types and condition of formation with reference to bars. Geographical Review of Japan 48, 712–730. doi:10.4157/grj. 48.712.
- Ikeda, H., 1983. Experiments on bedload transport, bed forms, and sedimentary structures using fine gravel in the 4-meter-wide flume. URL: https://www.ied.tsukuba.ac.jp/wordpress/--wpcontent/uploads/pdf_papers/ercpaper/erc2.pdf.
- Ikeda, S., 1984. Prediction of alternate bar wavelength and height. J. Hydraul. Eng. 110, 371–386. doi:10.1061/(ASCE)0733-9429(1984)110:4(371).
- Inoue, T., Watanabe, Y., Iwasaki, T., Otsuka, J., 2020. Three-dimensional antidunes coexisting with alternate bars. Earth Surf. Process. Landf. 45, 2897–2911. doi:10.1002/esp.4938.

- Iwasaki, T., Shimizu, Y., Kimura, I., 2016. Sensitivity of free bar morphology in rivers to secondary flow modeling: Linear stability analysis and numerical simulation. Adv. Water Resour. 92, 57–72. doi:10.1016/j.advwatres.2016.03.011.
- Jacobson, R.B., OConnor, J.E., Oguchi, T., 2016. Surficial geological tools in fluvial geomorphology. John Wiley & Sons, Ltd.: Chichester, UK. chapter 2. pp. 11–39. doi:10.1002/9781118648551.ch2.
- Jaeggi, M.N.R., 1984. Formation and effects of alternate bars. J. Hydraul. Eng. 110, 142–156. doi:10.1061/(ASCE)0733-9429(1984)110:2(142).
- Jeffreys, H.J., 1925. The flow of water in an inclined channel of rectangular section. Phil. Mag. 49, 793–807. doi:10.1080/14786442508634662.
- Julien, P.Y., 2010. Erosion and Sedimentation. Cambridge University Press, Cambridge. doi:10.1017/CB09780511806049.
- Karcz, I., Kersey, D., 1980. Experimental study of free-surface flow instability and bedforms in shallow flows. Sediment. Geol. 27, 263–300. doi:10.1016/0037-0738(80)90016-0.
- Kennedy, J.F., 1960. Stationary waves and antidunes in alluvial channels. California Institute of Technology. doi:10.7907/Y27F-NR79.
- Kennedy, J.F., 1963. The mechanics of dunes and antidunes in erodible-bed channels. J. Fluid Mech. 16, 521–544. doi:10.1017/S0022112063000975.
- Kennedy, J.F., 1969. The formation of sediment ripples, dunes, and antidunes. Annu. Rev. Fluid Mech. 1, 147–168. doi:10.1146/annurev.fl.01.010169.001051.
- Kinoshita, R., 1957. On the formation of river dunes, an observation on the meandering state. Transactions of JSCE 42, 243–258.
- Koskinas, A., Tegos, A., Tsira, P., Dimitriadis, P., Iliopoulou, T., Papanicolaou, P., Koutsoyiannis, D., Williamson, T., 2020. Insights into the Oroville dam 2017 spillway incident. Geosciences 9, 37. doi:10.3390/geosciences9010037.
- Kuroki, M., Kishi, T., 1984. Regime criteria on bars and braids in alluvial straight channels. Proceedings of the Japan Society of Civil Engineers 1984, 87–96. doi:10.2208/jscej1969. 1984.342_87.
- Lanzoni, S., 2000. Experiments on bar formation in a straight flume: 1. Uniform sediment. Water Resour. Res. 36, 3337–3349. doi:10.1029/2000WR900160.
- López, R., Barragán, J., 2008. Equivalent roughness of gravel-bed rivers. J. Hydraul. Eng. 134, 847–851. doi:10.1061/(ASCE)0733-9429(2008)134:6(847).
- Mahato, R.K., Ali, S.Z., Dey, S., 2021. Hydrodynamic instability of free river bars. Phys. Fluids 33, 045105. doi:10.1063/5.0045530.
- McLean, S.R., 1990. The stability of ripples and dunes. Earth-Sci. Rev. 29, 131–144. doi:10.1016/0012-8252(0)90032-Q.

- Mettra, F., 2014. Morphodynamic mechanisms in steep channels: from local processes to large-scale evolution. Ph.D. thesis. LHE/EPFL, Switzerland. doi:10.5075/epfl-thesis-6065.
- Möller, T., 1997. A fast triangle-triangle intersection test. J. Graph. Tools. 2, 25–30. doi:10.1080/10867651.1997.10487472.
- Moteki, D., Hiroyasu, Y., Seki, S., Hayasaka, K., Muramatsu, S., 2022. Data underlying the publication: Measured data of water surface and bottom on a sandbar. doi:10.4121/21201731. V1.
- Moteki, D.and Seki, S., Muramatsu, S., Hayasaka, K., Yasuda, H., 2023. On the occurrence of sandbars. Phys. Fluids 35, 016608. doi:10.1063/5.0128760.
- Muramoto, Y., Fujita, Y., 1977. Study on meso scale river bed configuration. Annuals, Disast. Prevo Res. Inst., Kyoto Univ. 20B-2, 243–258. In Japanese.
- Needham, D.J., Merkin, J.H., 1984. On roll waves down an open inclined channel. Proc. R. Soc. A 394, 259–278. doi:10.1098/rspa.1984.0079.
- Nelson, J.N., 1990. The initial instability and finite-amplitude stability of alternate bars in straight channels. Earth-Sci. Rev. 29, 97–115. doi:10.1016/0012-8252(0)90030-Y.
- Parker, G., 1976. On the cause and characteristic scales of meandering and braiding in rivers. J. Fluid Mech. 76, 457–480. doi:10.1017/S0022112076000748.
- Pascal, I., Ancey, C., Bohorquez, P., 2021. The variability of antidune morphodynamics on steep slopes. Earth Surf. Proc. Land. 46, 1750–1–765. doi:10.1002/esp.5110.
- Qian, H., Cao, Z., Liu, H., Pender, G., 2017. Numerical modelling of alternate bar formation, development and sediment sorting in straight channels. Earth Surf. Process. 42, 555–574. doi:10.1002/esp.3988.
- Recking, A., Bacchi, V., Naaim, M., Frey, P., 2009. Antidunes on steep slopes. J. Geophys. Res. Earth Surf. 114, F04025. doi:10.1029/2008JF001216.
- Redolfi, M., 2021. Free alternate bars in rivers: Key physical mechanisms and simple formation criterion. Water Resources Research 57, e2021WR030617. doi:10.1029/2021WR030617.
- Reynolds, A.J., 1965. Waves on the erodible bed of an open channel. J. Fluid Mech. 22, 113–133. doi:10.1017/S0022112065000630.
- Rhoads, B.L., 2020. The Dynamics of Braided Rivers. Cambridge University Press. doi:10.1017/9781108164108.010.
- Robillard, L., 1965. Free surface flow over a wavy bed. MSc. thesis. Massachusetts Institute of Technology, US. URL: http://hdl.handle.net/1721.1/13624.
- Schmid, P.J., Henningson, D.S., 2001. Stability and Transition in Shear Flows. Springer. doi:10.1007/978-1-4613-0185-1.
- Seki, S., Moteki, D., Yasuda, H., 2023. Novel hypothesis on the occurrence of sandbars. Phys. Fluids 35, 106611. doi:10.1063/5.0171731.

- Seminara, G., 2010. Fluvial sedimentary patterns. Annu. Rev. Fluid Mech. 42, 43–66. doi:10. 1146/annurev-fluid-121108-145612.
- Seminara, G., Lanzoni, S., Tambroni, N., 2023. Theoretical Morphodynamics: Straight Channels. Firenze University Press. doi:10.36253/979-12-215-0213-8.
- Shaw, J., Kellerhals, R., 1977. Paleohydraulic interpretation of antidune bedforms with applications to antidunes in gravel. J. Sediment. Res. 47, 257–266. doi:10.1306/212F7149-2B24-11D7-8648000102C1865D.
- Slootman, A., Cartigny, M.J.B., 2020. Cyclic steps: Review and aggradation-based classification Earth-Sci. Rev. 201, 102949. doi:10.1016/j.earscirev.2019.102949.
- da Silva, A.M.F., 1991. Alternate bars and related alluvial processes. Ph.D. thesis. M.Sc. Thesis, Department of Civil Engineering, Queens University, Kingston.
- da Silva, A.M.F., Yalin, M.S., 2017. Fluvial Processes. CRC Press. doi:10.4324/9781315206189.
- Simons, D.B., Richardson, E.V., Haushild, W.L., 1963. Some effects of fine sediment on flow phenomena. Water-Supply Paper 1498-G, U.S. Geol. Survey,. doi:10.3133/wsp1498G.
- Southard, J.B., Boguchwal, L.A., 1997. Bed configurations in steady unidirectional water flows. Part 2. Synthesis of flume data. J. Sed. Res. 60, 658–679. doi:10.1306/212F9241-2B24-11D7-8648000102C1865D.
- Thompson, T.H., 1968. Determination of discharge during pulsating flow. Water-Supply Paper 1869-D, U.S. Geol. Survey, doi:10.3133/wsp1869D.
- Valentine, E.M., Benson, I.A., Nalluri, C., Bathurst, J.C., 2001. Regime theory and the stability of straight channels with bankfull and overbank flow. J. Hydraul. Res. 39, 259–268. doi:10.1080/00221680109499829.
- Vanoni, V.A., 1974. Factors determining bed forms of alluvial streams. J. Hydraul. Div. 100, 363–377. doi:10.1061/JYCEAJ.0003906.
- Vesipa, R., Camporeale, C., Ridolfi, L., 2012. A shallow-water theory of river bedforms supercritical conditions. Phys. Fluids 24, 094104. doi:10.1063/1.4753943.
- Wainwright, J., Parsons, A.J., Cooper, J.R., Gao, P., Gillies, J.A., Mao, L., Orford, J.D., Knight, P.G., 2015. The concept of transport capacity in geomorphology. Rev. Geophys. 53, 1155–1202. doi:10.1002/2014RG000474.
- Wang, J., Zhang, K., Li, P., Meng, Y., Zhao, L., 2021. Hydrodynamic characteristics and evolution law of roll waves in overland flow. Catena 198, 105068. doi:10.1016/j.catena.2020.105068.
- Yalin, M.S., 1977. Mechanics of Sediment Transport. Pergamon Press.
- Yokokawa, M., Hasegawa, K., Kanbayashi, S., Endo, N., 2010. Formative conditions and sedimentary structures of sandy 3D antidunes: an application of the gravel step-pool model to fine-grained sand in an experimental flume. Earth Surf. Process. Landf. 35, 1720–1729. doi:10.1002/esp.2069.

- Yu, J., Kevorkian, J., 2000. Nonlinear evolution of small disturbances into roll waves in an inclined open channel. J. Fluid Mech. 243, 575–594. doi:10.1017/S0022112092002830.
- Zhao, C., Gao, J., Zhang, M., Zhanga, T., Wang, F., 2015. Response of roll wave to suspended load and hydraulics of overland flow on steep slope. Catena 133, 394–402. doi:10.1016/j.catena. 2015.06.010.
- Zhou, D., Mendoza, C., 2005. Growth model for sand wavelets. J. Hydraul. Eng. 131, 866–876. doi:10.1061/(ASCE)0733-9429(2005)131:10(866).